Nonlinear dispersion relationships and dissipative properties of damped metamaterials embedding bistable attachments

Tao Wang, Cyril Touzé, Haiqin Li, Qian Ding

Noname manuscript No.
(will be inserted by the editor)

Nonlinear dispersion relationships and dissipative properties of damped metamaterials embedding bistable attachments

Tao Wang · Cyril Touzé · Haiqin Li · Qian Ding

Received: date / Accepted: date

Abstract Damped metamaterials embedded with numerous micro-bistable attachments hold great potential in wave manipulation and vibration reduction. However, most of the studies are generally devoted to conservative systems, while neglecting a detailed analysis of wave attenuation mechanisms together with complex nonlinear dynamical phenomena. To address these limitations, the nonlinear dispersion relationships of metamaterials composed of internal bistable attachments, are here analysed numerically by combining the harmonic balance method and the extended periodic motion concept. The numerical methods, coupled with an arc-length continuation method, can obtain the dispersion spectrum, internal resonant branches, waveform, and damping ratio under any wave amplitude. Suitable post-processing also allows predicting both the local stability and the wave attenuation properties. To verify the effectiveness and accuracy of this algorithm and provide a comparison for multi-stable metamaterial, a mono-stable metamaterial with cubic-nonlinear resonators is taken as the first example. Then, the undamped dispersion properties and underdamped wave attenuation mechanisms in a nonlinear metamaterial composed of lattices with internal micro-bistable oscillators, are fully addressed using the proposed technique. The results underline that the metamaterial with embedded bistable oscillators has symmetric and asymmetric dispersion branches related to stable and unstable equilibrium points. For small amplitudes, the dynamics is governed by stable asymmetric dispersion solutions and exhibit linear dispersion behaviour with locally resonant bandgap. For medium amplitudes, the bandgap disappears, but only unstable dispersion branches remain over a broader frequency range, which may excite chaotic inter-well motion or targeted energy transfer, enabling a rapid attenuation of wave energy. Two kinds of responses are associated with 1:2/3/4/5 internal resonances from acoustic branches and S-shaped regions in symmetric optic branches. For large amplitudes, waves decay according to symmetric acoustic branches. Notably, regardless of wave amplitude, low-frequency waves always propagate due to extremely lightly damped asymmetric acoustic branches.

Keywords Wave propagation · Internal resonance · Dispersion property · Underdamped metamaterial · Bistable attachment

1 Introduction

The study of mechanical metamaterials originates from the locally resonant photonic crystal, typically referring to a specially designed periodic structure with micro-local resonators arranged internally [1–6]. Due to these microresonators and the structure's periodicity, the locally resonant metamaterial can generate low-frequency bandgaps [7], super absorption [8], extreme material parameters (negative mass density, negative elastic modulus) [9,10], negative refraction [11], and other extraordinary physical properties near the natural frequency of the resonator. In the high-frequency range, it forms a super wide bandgap to stop wave propagation through the Bragg scattering mechanism between the adjacent lattices [12,13]. Thanks to these

T. Wang · H.Q. Li · Q. Ding (✉)
Department of Mechanics, Tianjin University, Tianjin, 300072, China
E-mail: qding@tju.edu.cn

T. Wang · H.Q. Li · Q. Ding
Tianjin Key Laboratory of Nonlinear Dynamics and Control, Tianjin, 300072, China

C. Touzé
IMSIA, ENSTA Paris-CNRS-EDF-CEA, Institut Polytechnique de Paris, 828 Boulevard des Maréchaux, Paris, 91762 Palaiseau Cedex, France

unique characteristics, locally resonant metamaterials can manipulate wave propagation and have broad application prospects in passive vibration reduction [14,15] and noise control [16]. Compared to traditional vibration reduction techniques, using metamaterials embedded with distributed internal micro resonators offers obvious advantages in the civil, aerospace, and automotive industries.

The wave manipulation capability of linear resonant metamaterials at low frequencies primarily benefits from the locally resonant bandgap, which arises due to the out-of-phase motion between the lattice and its internal resonators. Since this mechanism shares properties with the well-known tuned mass damper, locally resonant metamaterials are subjected to the same limitation, effectively stopping wave propagation only within a very narrow frequency band. Recently, nonlinearities have been introduced into the construction of metamaterials, with an attempt to exploit typical nonlinear behaviours, such as hardening/softening nonlinearity [17,18] and energy transfer [19–21]; to widen the bandgap. Zhou *et al.* [22] developed a nonlinear metamaterial with an adjustable center frequency and width of the bandgap, using an inertia amplification device and a quasi-zero stiffness. Liu *et al.* [23] widened the low-frequency bandgap of a one-dimensional metamaterial by inducing geometric nonlinear inerters into the internal oscillator of lattices. Casalotti *et al.* [24] effectively reduced the first three resonances of metamaterial beam by combining nonlinear vibrators with different parameters. Fang *et al.* [25] successfully controlled the response amplitude of metamaterials under large vibrations by incorporating local resonators with gaps into the beam structure to generate chaotic bandgap. Subsequently, a low-frequency broad gap has been achieved for the purpose of vibration reduction, by connecting adjacent bandgaps through this chaotic bandgap [26]. Finally, a parameter optimization on cubic nonlinear metamaterials demonstrated how their performance can be significantly improved [27].

Bistable nonlinearity holds potential in enhancing the wave attenuation performance of metamaterials due to its rich nonlinear dynamic behaviours, such as intra/inter-well motions, multi-periodic/aperiodic responses, etc. Extensive references [28–33] have demonstrated that resonators constructed using bistable structures possess wider bandwidths and better energy capture capabilities compared to linear or monostable nonlinear ones. References [34] and [35] have utilized analytical and numerical techniques to investigate the nonlinear normal mode (NNM) and slow dynamics of bistable absorbers, also known as bistable nonlinear energy sinks (BNES), embedded in linear oscillators, respectively. These studies have demonstrated the potential of BNES in capturing and dissipating energy effectively. For instance, a magnetic vibration absorber has been designed in [36], where linear and nonlinear stiffnesses can be tuned thanks to the arrangements of the magnets, and the bistable case showed a good mitigation performance [37]. Recently, Al-Shudeifat *et al.* [38] have comprehensively explained the resonance capture mechanism of BNES, indicating that BNES primarily captures the energy of the main structure through chaotic inter-well motion and targeted energy transfer (TET). The application of BNES in locally resonant metamaterials has only gained attention in recent years. Xia *et al.* [39,40] designed a multi-stable metamaterial by periodically embedding micro BNESs inside a cantilever beam and found that the introduction of a bistable nonlinearity could effectively broaden low-frequency bandgap through the chaotic inter-well motion. To enhance the amplitude robustness, Xu *et al.* [41] combined bistable and mono-stable resonators to construct a novel metamaterial. Numerical simulations and experimental results revealed that this new metamaterial exhibits a more robust wide bandgap. Meng *et al.* [42] broaden the effective frequency range of a two-dimensional metamaterial by periodically embedding BNESs into sandwich plates. Zhang *et al.* [43] designed a metamaterial beam with internal two-degree-of-freedom bistable attachments and demonstrated its excellent vibration absorption performance. Although the vibration reduction performance of locally resonant metamaterials with internal BNESs has been confirmed, their wave manipulation and energy dissipation mechanisms are unclear. Moreover, existing references are based on finite structures, and the analysis for such complex systems with infinite degrees of freedom needs further discussion.

The dispersion spectrum serves as a crucial tool for unveiling the wave manipulation ability of metamaterials. For linear structures, the dispersion relationship can be derived by Bloch's theorem [44], which assumes that the variables at the lattice points satisfy periodic conditions. Utilizing such periodic boundary can simplify the lattice model, allowing the application of analysis techniques for finite structures to discuss the metamaterial's dispersion properties. Bloch's theorem is also widely applied to nonlinear problems. Shen *et al.* [45] discussed the dispersion spectrum of a honeycomb plate embedded with nonlinear resonators using Bloch's theorem and the method of multiple scales. Gong *et al.* [46] simplified the dynamic model of a triatomic nonlinear oscillator chain using periodic boundary conditions and revealed the evolution of dispersion characteristics with amplitude thanks to the harmonic balance method (HBM). For metamaterials with micro-internal bistable oscillators, these analysis techniques based on Bloch's theorem may not be always effective due to its rich internal resonant phenomena, which are not considered by Bloch's theorem. Most existing literature discusses the internal resonant behaviour of metamaterials using directly the method of

multiple scales [47–50] or analytic Hamiltonian perturbation approach [51,52]. Panigrahi *et al.* [49] discussed wave-wave interactions in oscillator chain models with quadratic and cubic nonlinearities based on multi-scale techniques, finding that internal resonance may occur when the frequencies and wavenumbers are in integer ratios. Fronk *et al.* [48] use the same approach to investigate energy exchange between plane waves in one-dimensional nonlinear metamaterial. Fortunati *et al.* [51] derived the invariant manifold of the internal resonant wave via the Hamiltonian perturbation approach. These analytic techniques can be applied for internal resonance problems, but are not suited for strongly nonlinear dynamics or global dynamics analysis. In this case, the HBM is an efficient numerical alternative. Narisetii *et al.* [53] modified the HBM to fit the infinite metamaterial without Bloch's assumption. In [53], they successfully transformed the lattice's nonlinear model into a set of algebraic equations by assuming the lattice displacement as a superposition of Bloch waves with multiple frequencies and wavenumbers. The dispersive properties of one-dimensional oscillator chains and two-dimensional lattices with Hertzian contacts are obtained using a Newton-like iterative algorithm.

When analysing the wave dispersion properties, the losses are generally overlooked, and the extension of the results to lightly damped metamaterials is assumed by continuity. This assumption however prevents from a quantitative study of the wave attenuation mechanism. Recently, references [54,55] have employed the method of multiple scales to incorporate the damping effects in nonlinear metamaterials, revealing that the wave frequency can shift as the amplitude decays, although the internal resonance scenario was excluded. In that context, one can make use of the extended periodic motion concept (EPMC) to achieve a quantitative analysis of the dissipative properties in the metamaterial exhibiting complex nonlinear behaviors. EPMC was first introduced by Krack [56], with the idea of extending the periodic orbit analysis of conservative systems to draw out the picture of damped NNMs [57,58]. The underlying idea is to introduce an artificial negative damping term into the damped system, acting as a source that counterbalances the energy dissipated during one period. Consequently, the modified system contains periodic orbit solutions that can be readily computed thanks to the HBM. EPMC is thus an *ad-hoc* yet straightforward technique, that has already been used in various damped systems [59–61]. Although primarily designed for damped NNMs in finite structures, the concept of using artificial damping to offset inherent damping easily extends to infinite metastructures. One must however bear in mind the intrinsic limitations of the method, which generally acts as an artificial calculation which is prone to retrieving the behaviour of the exact system in some specific cases only. Besides, the best accuracy is generally achieved for lightly damped systems, while the predictions given in the case of internal resonance are prone to further verifications. An alternative approach involving complex eigenvalue analysis has also demonstrated potential for addressing damped dispersion spectra. Arena *et al.* [62] developed a dynamical model for a viscoelastic metamaterial using the added-states technique and analyzed the damped linear dispersion spectrum and corresponding damping ratios by solving a polynomial eigenvalue problem. Although this method can be naturally extended to nonlinear cases, EPMC may provide superior accuracy, similar to its performance in finite structures [63,61].

As a summary, metamaterial with micro-internal nonlinear oscillators hold broad application prospects in low-frequency vibration reduction and wave manipulation. However, due to complex nonlinear behaviours, the wave manipulation and energy dissipation mechanism of infinite degree-of-freedom lightly damped metamaterials with internal bistable oscillators, have not been fully clarified yet. To fill this gap, this work provides numerical analysis techniques adapted to such structure and reveals the undamped dispersion properties and underdamped wave attenuation mechanisms in a metamaterial with micro-internal bistable attachement. In Sec. 2, the research objective, an infinite oscillator chain model composed of two-degree-of-freedom lattices with internal BNES, is introduced, and its dimensionless dynamic equations are presented. Section 3.1 introduces the EPMC, and section 3.2 exploits this approach to modify the direct HBM based on multi-frequencies and wavenumbers solution, hence providing a general treatment adapted to weakly damped, strongly nonlinear metamaterials. The revised HBM is referred to as EPMC-HBM in this paper. Notably, the numerical procedure is directly able to handle the case of undamped systems as a subcase. Section 3.3 details the process for computing numerical dispersion solutions from multi-stable metamaterial using EPMC-HBM and arc-length continuation technique [64]. In Sec. 3.4, two post-processing schemes are also presented to predict the local stability and wave attenuation characteristics. In Section 4.1, the monostable nonlinear metamaterial is taken as an example to validate the correctness of the proposed algorithm by comparing the results from EPMC-HBM and numerical intergration. The undamped multi-stable metamaterial is investigated to reveal its amplitude-dependent dispersion properties and rich internal resonance behaviours in Section 4.2. The wave attenuation mechanisms are then discussed in Section 4.3. Finally, Section 5 summarizes the main contributions of this work.

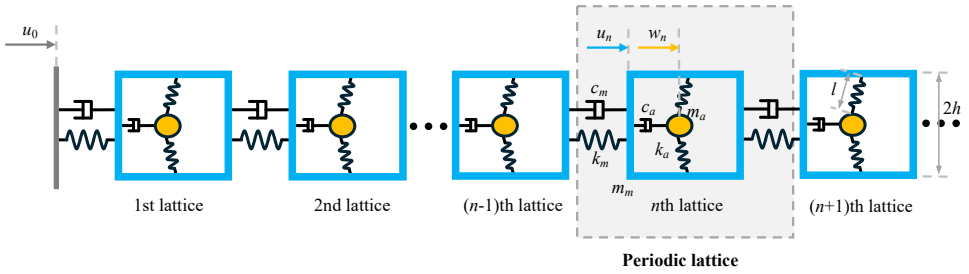

Fig. 1 Schematic representation of the one-dimensional lightly damped multi-stable metamaterial composed of two-degree-of-freedom lattices with internal bistable attachments.

2 Equations of motion

The schematic diagram of the underdamped metamaterial with internal bistable attachments is shown in Fig. 1. It is a one-dimensional infinite oscillator chain model, composed of an arrangement of a main linear oscillator and an internal nonlinear resonator. Each lattice comprises an external host mass element m_m and an internal micro bistable attachment m_a. The masses m_m and m_a are connected through a nonlinear spring with linear damping c_a, whereas adjacent lattices are linked via a linear stiffness k_m and viscous damping c_m. The first lattice is connected to a rigid body moving with $u_0 = A\cos\omega_e t$ to input energy. The bistable spring between m_m and m_a is realized by vertically arranging a pair of pre-compressed linear springs characterized by stiffness k_a and natural length l. Assuming that the height of the external mass block is $2h$, subsequently ensuring $l > h$, such that the springs are pre-compressed, allows one to write the restoring force as:

$$f_n = \frac{2k_a\left(w_n - u_n\right)}{\sqrt{h^2 + \left(w_n - u_n\right)^2}}\left(\sqrt{h^2 + \left(w_n - u_n\right)^2} - l\right), \tag{1a}$$

$$= \sum_{n=1} k_{a(2n-1)}\left(w_n - u_n\right)^{2n-1}, \tag{1b}$$

where

$$k_{a1} = -\frac{2k_a(l-h)}{h}, k_{a3} = \frac{k_a l}{h^3}, \ldots$$

and u_n, w_n represent the displacements of m_m and m_a in the n-th lattice, respectively. While Eq. (1a) refers to the exact expression of the restoring force, Eq. (1b) exhibits its Taylor expansion by assuming small motions. In this study, the Taylor expansion is truncated to the third-order, since the primary objective is to elucidate the influence of bistable characteristics on wave propagation. Such an effect can be accurately characterized by a combination of a negative linear stiffness k_{a1}, and a positive cubic stiffness k_{a3}. Note that the effect of the truncation is further examined in Appendix A, by comparing the dispersion spectrum derived from exact and approximate models, underlining that, in the range of amplitudes considered, the third-order truncation provides sufficiently accurate results.

With these assumptions, the equations of motion of the metamaterial read, $\forall n \geq 1$:

$$m_m\frac{\mathrm{d}^2u_n}{\mathrm{d}t^2} + 2c_m\frac{\mathrm{d}u_n}{\mathrm{d}t} + 2k_m u_n - c_m\frac{\mathrm{d}\left(u_{n-1}+u_{n+1}\right)}{\mathrm{d}t} - k_m\left(u_{n-1}+u_{n+1}\right) + m_a\frac{\mathrm{d}^2w_n}{\mathrm{d}t^2} = 0, \tag{2a}$$

$$m_a\frac{\mathrm{d}^2w_n}{\mathrm{d}t^2} + c_a\frac{\mathrm{d}\left(w_n-u_n\right)}{\mathrm{d}t} + k_{a1}\left(w_n-u_n\right) + k_{a3}\left(w_n-u_n\right)^3 = 0, \tag{2b}$$

where t denotes the time, and $n \geq 1$ represents the lattice number. To simplify the analysis, the following dimensionless parameters are introduced:

$$\varepsilon = \frac{m_a}{m_m}, \omega_m = \sqrt{\frac{k_m}{m_m}}, \lambda_m = \frac{c_m}{m_m\omega_m}, \tau = \omega_m t, A_d = \frac{A}{x_0}, \omega_{de} = \frac{\omega_e}{\omega_m}, \tag{3a}$$

$$u_{dn} = \frac{u_n}{x_0}, w_{dn} = \frac{w_n}{x_0}, \lambda_a = \frac{c_a}{\varepsilon m_m\omega_m}, \kappa = \frac{k_{a1}}{\varepsilon m_m\omega_m^2}, \gamma = \frac{k_{a3}x_0^2}{\varepsilon m_m\omega_m^2}. \tag{3b}$$

The characteristic length used here to make the displacements nondimensional is arbitrarily selected as $x_0 = m_m g/k_m$, where g denotes the gravitational acceleration, equal to 9.8 m/s^2. To simplify the equations of

motion, the relative displacement between the nondimensional displacements w_{dn} and u_{dn} is also introduced as:

$$v_{dn} = w_{dn} - u_{dn}, \tag{4}$$

Substituting Eqs. (3) and (4) into (2), yields the dimensionless dynamic model as:

$$(1+\varepsilon)\ddot{u}_{dn} + \varepsilon\ddot{v}_{dn} + 2\lambda_m\dot{u}_{dn} + 2u_{dn} - \lambda_m\left(\dot{u}_{dn-1} + \dot{u}_{dn+1}\right) - \left(u_{dn-1} + u_{dn+1}\right) = 0, \tag{5a}$$

$$\varepsilon\ddot{v}_{dn} + \varepsilon\lambda_a\dot{v}_{dn} + \varepsilon\kappa v_{dn} + \varepsilon\gamma v_{dn}^3 = -\varepsilon\ddot{u}_{dn}, \tag{5b}$$

where the usual notation $\dot{()}$ and $\ddot{()}$ has been used to represent first- and second-order derivations with respect to the dimensionless time τ. For the first lattice $n = 1$, u_{d0} refers to the displacement excitation at the leftmost end of the model shown in Fig.1, expressed as

$$u_{d0} = A_d \cos\omega_{de}\tau. \tag{6}$$

The parameters κ and γ in Eqs. (5) are key, as they dictate the behaviour of the internal oscillators. In the bistable scenario of interest, κ and γ are respectively assumed to have negative and positive values, due to the pre-compressed vertical spring ($l > h$ and $k_{a1} < 0$), leading to a bistable lattice featuring two stable non-trivial equilibrium points ($(u_{dn}, v_{dn}) = (0, \pm E_0)$, where $E_0 = \sqrt{-\kappa/\gamma}$), and one unstable trivial equilibrium point, $(u_{dn}, v_{dn}) = (0, 0)$. The presence of multiple equilibrium points underpins the exceptional ability of bistable systems to capture and dissipate the vibration energy.

3 Numerical analysis methods

To clarify the effect of the internal bistable oscillator in wave manipulation and attenuation, this section introduces a numerical analysis framework based on EPMC and the HBM with multiple frequencies and wavenumbers solutions. The equations of motion are first rewritten in a general formulation as:

$$\mathbf{M}\ddot{\mathbf{x}}_n + \sum_{i=-1}^{1}\mathbf{C}_i\dot{\mathbf{x}}_{n+i} + \sum_{i=-1}^{1}\mathbf{K}_i\mathbf{x}_{n+i} + \mathbf{F}_n\left(\mathbf{x}_n\right) = \mathbf{0}, \tag{7}$$

where the following terms have been introduced:

$$\mathbf{x}_n = \begin{bmatrix} u_{dn} \\ v_{dn} \end{bmatrix}, \mathbf{M} = \begin{bmatrix} 1+\varepsilon & \varepsilon \\ \varepsilon & \varepsilon \end{bmatrix}, \mathbf{C}_0 = \begin{bmatrix} 2\lambda_m & 0 \\ 0 & \varepsilon\lambda_a \end{bmatrix}, \mathbf{K}_0 = \begin{bmatrix} 2 & 0 \\ 0 & \varepsilon\kappa \end{bmatrix}, \tag{8a}$$

$$\mathbf{C}_{\pm1} = \begin{bmatrix} -\lambda_m & 0 \\ 0 & 0 \end{bmatrix}, \mathbf{K}_{\pm1} = \begin{bmatrix} -1 & 0 \\ 0 & 0 \end{bmatrix}, \mathbf{F}_n = \begin{bmatrix} 0 \\ \varepsilon\gamma v_{dn}^3 \end{bmatrix}. \tag{8b}$$

To derive the dispersion spectrum for such lattices and handle the variables from adjacent cells, Bloch's theorem has been used in several different studies, see *e.g.* [2,46]. However, underlying assumptions might fall in cases where nonlinear behaviours including for example internal resonance, are taken into account. To that purpose, the Harmonic Balance Method (HBM) provides an effective numerical tool that can be easily used for computing dispersion curves for undamped systems. To enlarge the scope of the analysis to damped systems and more finely analyse the dissipative properties, the EPMC is used in conjunction with the HBM. The next Sections aim to explain how these techniques are deployed together with an arc-length continuation procedure to offer an integrated numerical bench for the analysis.

3.1 Extended Periodic Motion Concept

The EPMC was initially used to obtain the damped NNMs of nonlinear structures [56]. The essential idea involves adding an artificial negative damping term to a damped system for balancing the energy dissipated over one period, turning the original dissipative system into a self-excited system. The periodic orbits of the self-excited system are the extended periodic motions of the original one. Such modified system can be solved using traditional techniques for undamped systems, such as HBM or the shooting technique. Although this approach primarily targets damped NNM, considering the NNM is very similar to the dispersion solution, transferring this energy balancing idea to damped metamaterial raises no difficulty.

According to [56], the artificial negative damping term $-2\zeta\omega\mathbf{M}\dot{x}_n$ is added to Eq. (7) for maintaining the existence of traveling wave solutions

$$\mathbf{M}\ddot{\mathbf{x}}_n + \sum_{i=-1}^{1}\mathbf{C}_i\dot{\mathbf{x}}_{n+i} - 2\zeta\omega\mathbf{M}\dot{\mathbf{x}}_n + \sum_{i=-1}^{1}\mathbf{K}_i\mathbf{x}_{n+i} + \mathbf{F}_n\left(\mathbf{x}_n\right) = \mathbf{0}, \tag{9}$$

where ζ and ω represent the damping ratio and frequency of the dispersion solution, respectively. There are two unknown parameters to be determined during the computation of the dispersion solutions. Interestingly, one can very easily use the same framework to compute also the periodic solutions of the conservative underlying system, by simply setting $\mathbf{C}_i = \mathbf{0}$, and the damping ratio ζ will automatically balance to zero when solving for Eq. (9).

As stated from Eq. (9), the EPMC aims at controlling the damped system with a single scalar ζ in a mass-proportional viscous damping. While such a strong assumption has proven effective for lightly damped systems, its application to correctly represent the nonlinear dynamics of a dissipative system with large damping values is questionable. Also, other important cases such as the occurrence of internal resonance and/or the presence of a nonlinear damping law, highlight why EPMC might fall short in difficult cases. For all these reasons, dispersion spectrum analysis will primarily focus on the conservative models in this article. The EPMC will then be used only to offer a better understanding and a quantitative prediction of the wave attenuation mechanism when light damping is taken into account. Finally, since the framework easily adapts to undamped systems, it is applied to both cases. The HBM and its companion arc-length continuation technique are presented in the next sections for the damped case for the sake of completeness.

3.2 Harmonic Balance Method

The HBM is used to solve for Eq. (9). According to [53], the response can be sought as

$$\mathbf{x}_{n+i} = a\left[\mathbf{A}_0 + \sum_{m=1}^{H} \frac{\mathbf{A}_m}{2} e^{jm(\omega\tau - ki)}\right] + c.c., \tag{10}$$

where $\mathbf{A}_m$ represents the m-th order harmonic coefficient, a controls the wave amplitude, k denotes wavenumber, j is the imaginary unit, H denotes the number of harmonics, and *c.c.* stands for complex conjugate. Substituting Eq. (10) into (9) yields:

$$\begin{array}{l} a\left[\sum_{m=1}^{H}\left(-m^2\omega^2\mathbf{M} + jm\omega\big(\mathbf{C}_0 - 2\zeta\omega\mathbf{M} + 2\cos(mk)\mathbf{C}_{-1}\big) + \mathbf{K}_0 + 2\cos(mk)\mathbf{K}_{-1}\right)\frac{\mathbf{A}_m}{2}e^{jm\omega\tau}\right. \\ \left. + \sum_{m=-1}^{1}\mathbf{K}_m\mathbf{A}_0\right] + \sum_{m=0}^{H}\mathbf{f}_{nm}e^{jm\omega\tau} + c.c. = \mathbf{0}, \end{array} \tag{11}$$

where $\mathbf{f}_{nm}$ is the m-th order harmonic coefficient of $\mathbf{F}_n$, which can be obtained through the Fourier transform as:

$$\mathbf{f}_{nm} = \frac{\omega}{2\pi}\int_0^{\frac{2\pi}{\omega}} \mathbf{F}_n\left(\mathbf{x}_n\right) e^{-jm\omega\tau} d\tau. \tag{12}$$

Balancing the harmonics in Eq. (11), a set of algebraic equations reading $\mathbf{R}_c = \mathbf{0}$, is obtained, with

$$\mathbf{R}_c = a\left[-\omega^2\nabla^2 \otimes \mathbf{M} + j\omega\left(\nabla \otimes (\mathbf{C}_0 - 2\zeta\omega\mathbf{M}) \;\; + 2\nabla\nabla_k \otimes \mathbf{C}_{-1}\right) + \mathbf{I} \otimes \mathbf{K}_0 + 2\nabla_k \otimes \mathbf{K}_{-1}\right]\mathbf{A} + \mathbf{F}_{nH}, \tag{13}$$

where the symbol $\otimes$ stands for the Kronecker product [65,66], and the following notations have been introduced:

$$\nabla = \mathrm{diag}\left(\left[\begin{array}{cccc} 0 & 1 & 2 & \cdots \;\; H \end{array}\right]\right), \tag{14a}$$

$$\nabla_k = \mathrm{diag}\left(\left[\begin{array}{cccc} 1 & \cos k & \cdots & \cos Hk \end{array}\right]\right), \tag{14b}$$

$$\mathbf{A} = \left[\mathbf{A}_0^{\mathrm{T}}, \frac{\mathbf{A}_1^{\mathrm{T}}}{1}, \cdots, \frac{\mathbf{A}_H^{\mathrm{T}}}{2}\right]^{\mathrm{T}}, \tag{14c}$$

$$\mathbf{F}_{nH} = \left[\mathbf{f}_{n0}^{\mathrm{T}}, \mathbf{f}_{n1}^{\mathrm{T}}, \cdots, \mathbf{f}_{nH}^{\mathrm{T}}\right]^{\mathrm{T}}. \tag{14d}$$

Eq. (13) consists of $(1+H)n$ algebraic equations and contains $(1+H)n+4$ unknown variables, which are $\mathbf{A}$, ω, ζ, a, and k. To ensure that the dispersion solutions can be determined when a and k are fixed, two additional constraints are introduced as:

$$\mathbf{R}_1 = \mathrm{Re}\left(\sum_{m=0}^{H} \mathbf{A}_m^{\mathrm{H}}\mathbf{M}\mathbf{A}_m\right) - 1 = 0, \tag{15}$$

$$\mathbf{R}_2 = \sum_{m=1}^{H} m\mathrm{Im}\left(\mathbf{A}_m\left(i_{norm}\right)\right) = 0. \tag{16}$$

Eq. (15) is used to ensure that the wave amplitude is uniquely controlled by the introduced amplitude a, while Eq. (16) is used to fix the initial phase of the travelling wave. In Eq. (16), i_{norm} represents the physical degree of freedom where the phase has been fixed. This location is arbitrary.

Combining Eqs. (13) - (16), a new residual equation can be derived

$$\mathbf{R}(\mathbf{A}, \omega, \zeta, k, a) = \begin{bmatrix} \mathbf{R}_c \\ \mathbf{R}_1 \\ \mathbf{R}_2 \end{bmatrix} = \mathbf{0}. \tag{17}$$

Eq. (17) can determine a dispersion spectrum related to a given wave amplitude and wavenumber. Among the equation's components, $\mathbf{f}_{nm}$ poses the most significant challenge in terms of computation. For a straightforward nonlinear restoring force $\mathbf{F}_n$, like the approximate cubic nonlinear force considered in this study, the $\mathbf{f}_{nm}$ can be analytically derived from Eq. (12). However, for more difficult cases, such as the exact square root nonlinearity, this approach becomes cumbersome. In such a case, the Alternating-Frequency-Time (AFT) scheme can be used as an efficient alternative [67]. Hence, even though the EPMC-HBM scheme proposed herein will be used only for a cubic nonlinearity, it can be easily generalized to a broad range of nonlinearities.

A last point is worth mentioning. The main primary oscillator in the model considered does not contain a nonlinear stiffness term. Hence, the first equation in (17), which is the residual equation for the direct current component of the first degree of freedom, becomes trivial, stating $0 = 0$. Consequently, Eqs. (17) describe an infinite number of waveforms at one dispersion solution, and each waveform has a different static bias $\mathbf{A}_0(1)$. Considering this static bias does not affect the dispersion properties, and one can simply assume $\mathbf{A}_0(1) = 0$. The case of a nonlinear primary oscillator can also be treated by the present numerical approach. For the sake of completeness, Appendix B shows such an example.

3.3 Numerical Continuation Procedure

As mentioned before, Eq. (17) can determine a two-dimensional manifold expressing the nonlinear dispersion relationships as a function of both the amplitude a and the wavenumber k. However, solving for this manifold presents another challenge. By fixing a and k, the corresponding dispersion solutions can be obtained using a Newton-like iterative procedure [53]. But this approach has two critical drawbacks: on the one hand, the convergence of the Newton-like iterative algorithm highly depends on the initial guesses; on the other hand, the algorithm often fails to deal with manifold folding. Therefore, it is only suitable for cases where the dispersion manifold has a simple geometry.

To address this problem, numerical continuation techniques are routinely used in the field of nonlinear dynamics. It is important to note that numerical continuation methods are primarily suitable for path following along a single scalar continuation parameter. In this paper, we opt to fix the wavenumber k and continue in amplitude a. The numerical computation of the nonlinear dispersion curves using arc-length continuation thus follows the five steps below:

Step 1: a wavenumber k is selected together with a small initial amplitude a_p. Thanks to the linear dispersion analysis, the harmonic coefficients $\mathbf{A}_p$ and ω_p can be obtained. Considering the system as weakly damped, assume the damping ratio $\zeta_p = 0$. Based on the chosen initial values, the initial prediction point can be given as $\mathbf{p}_0^p = [\mathbf{A}_p^{\mathrm{T}}, \omega_p, \zeta_p, a_p]^{\mathrm{T}}$.

Step 2: Next, a constraint equation $c_a(a) = a - a_p = 0$ is introduced and combined with Eq. (17), yielding $\mathbf{R}_{e1} = [\mathbf{R}; c_a] = \mathbf{0}$. Taking $\mathbf{p}_0^p$ as the initial condition and solving for this equation using a Newton-like iterative algorithm, one obtains $\mathbf{p}_0$ for a_p. This $\mathbf{p}_0$ serves as the starting point for numerical continuation.

Step 3: Assuming that the i-th point $\mathbf{p}_i$ is known, a two-step procedure including prediction and correction, is devised to find the next point $\mathbf{p}_{i+1}$. For prediction, it requires the knowledge of the tangent vector of the one-dimensional manifold at $\mathbf{p}_i$. To obtain this vector, an arc-length parameter s is introduced. By differentiating Eq. (17) with respect to s, the tangent vector can be derived as

$$\frac{\partial \mathbf{R}}{\partial \mathbf{p}} \frac{\partial \mathbf{p}}{\partial s} = \mathbf{0} \tag{18a}$$

$$\boldsymbol{\nu} = \frac{\partial \mathbf{p}/\partial s}{|\partial \mathbf{p}/\partial s|}, \tag{18b}$$

where $\boldsymbol{\nu}$ is the normalized tangent vector. The $\partial\mathbf{R}/\partial\mathbf{p}$ is the gradient of residual equation. The linear term can be analytically derived, while the computation of the nonlinear part can be done either analytically or with the AFT technique. [67]. Finally, the predicted $i+1$th point can be written as

$$\mathbf{p}_{i+1}^{p} = \mathbf{p}_i + \boldsymbol{\nu}\Delta s \tag{19}$$

where Δs denotes the step length of the continuation.

Step 4 is the correction step. To ensure that the $i+1$th and ith solutions maintain a constant arc-length Δs during the correction process, another constraint equation needs to be introduced: $c_s(\mathbf{p}|\mathbf{p}_i, \Delta s) = (\mathbf{p}-\mathbf{p}_i)^{\mathrm{H}}(\mathbf{p}-\mathbf{p}_i) - \Delta s^2 = 0$. Combining this constraint equation with Eq. (17), yields $\mathbf{R}_{e2} = [\mathbf{R}; c_s] = \mathbf{0}$. Using $\mathbf{p}_{i+1}^{p}$ as the initial condition and solving for the equation with a Newton procedure, $\mathbf{p}_{i+1}$ is obtained. Repeat Steps 3 and 4 until the vector $\mathbf{p}_i$ meets the termination condition, and the one-dimensional manifold for fixed k can be acquired.

Step 5: By selecting different values of k within the irreducible Brillouin zone $0 < k < \pi$, and carrying out Steps 1-4, the dispersion properties of the metamaterial under various wavenumbers and wave amplitudes can be obtained.

3.4 Local Stability and Wave Attenuation Equation

Using EPMC-HBM introduced in Sections 3.1 – 3.3, the conservative as well as the underdamped dispersion relationships of the metamaterial with an internal nonlinear bistable oscillator, can be numerically obtained. To reveal its rich nonlinear behaviour and wave attenuation mechanism, it is still necessary to provide some post-processing methods.

To compute the local stability, an evaluation technique based on Floquet theory and Hsu's method [68], is used. The monodromy matrix $\mathbf{S}(k)$ is numerically obtained and the maximum absolute value λ_{max} of its eigenvalues within the range: $0 < k < \pi$, is determined to characterize the stability of numerical dispersion solutions. When $\lambda_{max} > 1$, the dispersion solution is unstable, otherwise, it is stable. The monodromy matrix can be expressed as

$$\mathbf{S}(k) = \prod_{i=1}^{N_t} \mathbf{S}_i(k) \tag{20}$$

where

$$\mathbf{S}_i(k) = \exp\left(\frac{2\pi}{\omega N_t}\mathbf{B}\left(\tau_{i-1}, k\right)\right), \tag{21a}$$

$$\mathbf{B} = \begin{bmatrix} \mathbf{0} & \mathbf{I} \\ -\mathbf{M}^{-1}\left(\mathbf{K}_0 + 2\cos k\mathbf{K}_{-1} + \partial\mathbf{F}_n\left(\mathbf{x}_n^0\right)/\partial\mathbf{x}_n\right) & -\mathbf{M}^{-1}\left(\mathbf{C}_0 - 2\zeta\omega\mathbf{M} + 2\cos k\mathbf{C}_{-1}\right) \end{bmatrix}. \tag{21b}$$

The $\mathbf{x}_n^0$ is the numerical dispersion solutions from EPMC-HBM. The derivation process of the $\mathbf{S}(k)$ and more details about the stability evaluation technique are given in Appendix C.

Regarding the wave attenuation process, it can be predicted by

$$\mathbf{x}_{n+i} = a_0 e^{-\zeta\omega\tau}\left(\mathbf{A}_0 + \sum_{m=1}^{H}\frac{\mathbf{A}_m e^{jm(\omega\tau - ik + \theta_s)}}{2} + c.c.\right), \tag{22}$$

where the ω, ζ, and $\mathbf{A}_m$ are all the functions of wave amplitude $a = a_0 e^{-\zeta\omega\tau}$. This functional relationship can be established by interpolating the results of numerical continuation. Eq. (22) can be derived by using a complex averaging method, as presented in Appendix C. Notably, Eq. (22) is only effective when no internal resonance is excited.

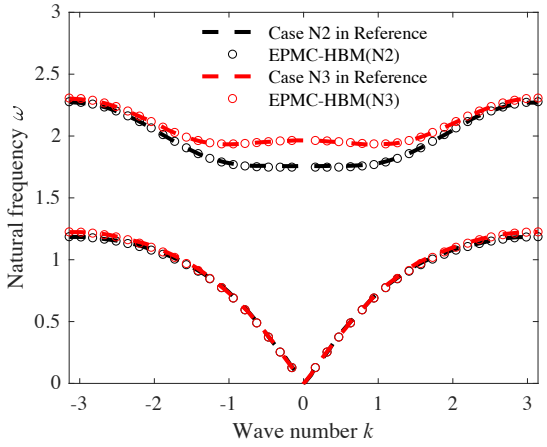

Fig. 2 Dispersion relationship for an undamped mono-stable metamaterial using the parameter values of reference [69]. Comparison between the results shown in [69] (dashed lines) and the outputs of the present numerical scheme (circles).

4 Numerical results

In this section, a comprehensive discussion will be conducted to understand the behaviours of the bistable metamaterials regarding the nonlinear dispersion relationships and dissipative properties using EPMC-HBM framework developed in Sec. 3. To this end, a mono-stable metamaterial with cubic-nonlinear resonators, is first analysed in Sec. 4.1 to serve as a reference example. Then in Sec. 4.2, the undamped dispersion properties and rich internal resonant behaviours of nonlinear metamaterial with internal bistable attachment, is analysed. Finally, considering the effect of damping, the wave attenuation process in this multi-stable metamaterial is investigated in Sec. 4.3.

It is noted that all the numerical integration results will be carried out based on a finite oscillator chain model consisting of 550 elements. The displacement excitation u_{d0} is applied to the leftmost end of the oscillator chain, as shown in Fig. 1. Additionally, the last 50 elements on the right end are supplemented with an exponentially increasing damping law, to prevent any wave reflection. To create this numerical anechoic termination, the damping terms of both the main and internal oscillators have been supplemented by an additional power law for the last 50 cells. The practical implementation is realized by imposing as damping factors $\lambda_m(n) = \lambda_m(n \leq 500) + C_{add}(n)$ and $\lambda_a(n) = \lambda_a(n \leq 500) + \varepsilon C_{add}(n)$, where the artificially added damping reads: $C_{add}(n) = C_{max}(n - 500)^p/50^p$. In the numerical simulations, the following values have been selected: $C_{max} = 1$, $p = 5$, and $\varepsilon = m_a/m_m = 0.1$ using the values given in Table 2. The following numerical parameters have also been set for all the results shown: 50 different wavenumbers, $k = n\pi/50, n = 1, 2, \cdots, 50$ are used in the EPMC-HBM framework, and the number H of harmonics for the HBM and continuation procedure is set to 5.

4.1 Numerical validation for a metamaterial with mono-stable nonlinear resonators

4.1.1 Undamped Case

To verify the effectiveness of the numerical procedures and to provide a point of comparison with the bi-stable case, a metamaterial with a cubic mono-stable nonlinear attachment, is first analysed. Its configuration and dynamic equations are the same as those of the multi-stable metamaterial introduced in Sec. 2, except that the linear stiffness is positive: $\kappa > 0$. To start with, the undamped case is investigated, such that c_m and c_a are set to 0 N·s/m.

The numerical EPMC-HBM scheme is first validated by comparing the dispersion relationships with those reported in [69]. The results are shown in Fig. 2. Two different cases are tested, respectively denoted as N2 and N3, where only the value of the nonlinear stiffness of the internal oscillator k_{a3} is modified, see Table 1, following the tuning proposed in [69]. It is found that the nonlinear dispersion properties show a perfect agreement, for both the acoustic and the optic branch.

Now returning to the mono-stable lattice, with the parameters given in Table 2, Fig. 3(a) displays the nonlinear dispersion relationship in the space of wavenumber-frequency-amplitude. Because of the nonlinearity, the dispersion spectrum depends on amplitude, and stable as well as unstable branches can be found.

Table 1 The parameters used in [69].

Primary oscillator	Internal oscillator
$m_m = 0$	$m_a = 0.5$
$c_m = 0$	$c_a = 0$
$k_m = 10\pi$	$k_{a1} = 7.5\pi$
$A = 5 \times 10^{-3}$	$k_{a3} = 5 \times 10^4$ (N2)
	$k_{a3} = 1 \times 10^5$ (N3)

Table 2 The parameters used for the mono-stable metamaterial.

Primary oscillator	Internal oscillator
$m_m = 0.1$ kg	$m_a = 0.01$ kg
$k_m = 100$ N/m	$k_a = 500$ N/m
$h = 0.05$ m	$l = 0.0499$ m

This two-dimensional dispersion manifold is composed of a collection of backbone curves representing the amplitude-frequency relationship of the wave with a fixed wavenumber k. As mentioned before, 50 different wavenumbers have been used to produce the result which is obtained by the combined EPMC-HBM procedure, and the stability of the resulting branches has been computed and reported with black dots for stable branches and red dots for unstable solutions. By slicing through this nonlinear dispersion manifold, one can conveniently extract the dispersion characteristics of the metamaterial for a given wave amplitude. To better illustrate the dependence upon amplitude, three cross-sections, respectively at the displacement amplitudes $u_{dn} = 1 \times 10^{-4}$, 0.1, and 0.5, are selected and shown in Figs. 3(b-c). The Fourier spectra of direct numerical integrations of the equations of motion, are also represented in Figs. 3(b-c) for comparison. These numerical results have been obtained by applying a 500 dimensionless time chirp excitation to the left end of the finite oscillator chain model (excitation amplitude $A_d = 1 \times 10^{-4}$, 0.1, and 0.5, ω_{de} increasing from 0.01 to 2.5), and then collecting data of $\dot{v}_{dn}$ from the 10th to 450th elements for a 2D FFT. It is worth noting that the wave's amplitude can be described by u_{dn} and A_d. To avoid confusion, we uniformly use A_d to characterize the wave amplitude, regardless of the results commented on (dispersion spectrum and direct numerical integration). Fig. 3 (b) allows recovering the linear dispersion spectrum by setting $A_d = 1 \times 10^{-4}$. Besides, direct numerical integration fits perfectly well with the numerical solution branches predicted with EPMC-HBM.

When A_d reaches an amplitude of 0.1, see Fig. 3(c), additional tongues appear in the acoustic branch, which intersect precisely with the optic branch with 1/3 frequency and wavenumber, suggesting that they are related to the 1:3 internal resonance between acoustic and optic branches. In the frequency range $0.45 < \omega < 0.7$, only unstable solution branches are found in the dispersion spectrum. As a consequence, the numerical two-dimensional Fourier spectrum is dispersed across the entire wavenumber domain. The unstable response is associated with the 1:3 internal resonance as shown in Fig. 3(e), the time-frequency diagram of 20th cell by fixing $\omega_{de} = 0.55$. Outside this particular interval, stable solution branches exist, and the numerical 2D Fourier spectrum precisely overlaps with the dispersion curve.

For $A_d = 0.5$, the dispersion spectrum predicted by EPMC-HBM reflects stable responses within a very low frequency and wavenumber range only, which is the consequence of the weak nonlinear restoring force associated to a small amplitude relative motion between the external and internal oscillators, parametrized by v_{dn}. When ω is beyond 0.3 but no more than 0.6, an unstable acoustic branch, with a relatively concentrated 2D Fourier spectrum, appears. Its response is shown in Fig. 3(f), where v_{d20} shows obvious high-frequency components in 300 to 500 dimensionless time, while u_{d20} still displays a periodic response. In the large unstable region for $\omega > 0.6$, the analysis of the 2D Fourier spectrum suggests a coupling between the unstable acoustic and optic branches. This coupling is also observed in subsequent multi-stable cases (see later in Figs. 9(b) and 13(c)), and will be further commented on in the next sections, in particular for the ability of such dynamical solution to favour targeted energy transfer (TET). Indeed, the typical S-shape of the backbone curves observed in Fig. 3(a) is the key to creating strongly modulated responses and TET [21]. This process is here just briefly mentioned, but is fully analysed in Section 4.2, since the same phenomenon is observed for a lattice with bistable attachments. From the above simulations, it can be concluded that the EPMC-HBM can accurately predict the dispersion properties of undamped metamaterials across various wave amplitudes, and the proposed post-processing techniques can also correctly mark the stability of dispersion solutions.

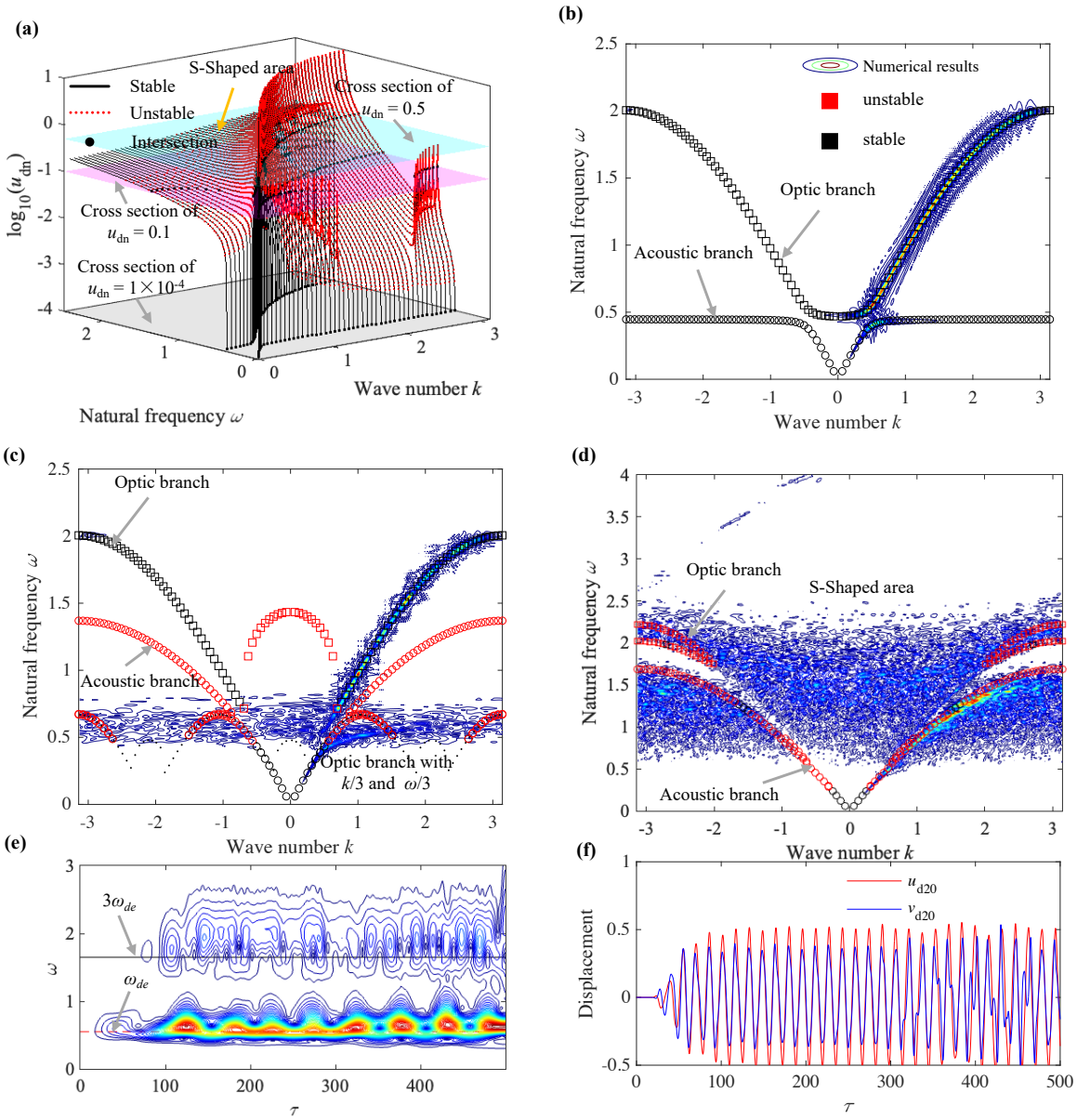

Fig. 3 Nonlinear dispersion characteristics for the undamped mono-stable metamaterial. (a) Two-dimensional dispersion manifold constructed by computing the amplitude-frequency relationships for different wavenumbers. (b-d) Comparison of nonlinear dispersion relationships obtained from EPMC-HBM with direct numerical integration, for three increasing amplitudes: (b) A_d=1×10^{-4}, (c) A_d=0.1, and (d) A_d=0.5. The optic branch is represented by squares, while the acoustic branch with circles. Stable parts in black and unstable parts in red. In (c), the 1/3 optic branch where both frequency and wavenumber have been divided by three, is represented with black points. (e-f) time-frequency diagram and time-domain response of the 20th cell when selecting: (e) $\omega_{de}=0.55$ for $A_d=0.1$ and (f) $\omega_{de}=0.4$ for $A_d=0.5$.

4.1.2 Lightly damped case

The case of a lightly damped chain is now considered by setting the damping values of the primary and inner oscillators as $c_m = 0.01$ N·s/m, $c_a = 0.02$ N·s/m. The excitation used for numerical integration is applied at the left end of the oscillator chain, lasting for 500 dimensionless time instants with $\omega_{de} = 0.355$. To mitigate the influence of the transient response during wave propagation, A_d is exponentially increased from 0 to $0.99A_{d0}$ over 8 loading periods and then asymptotically approaches A_{d0} with time. Such A_d can be represented as

$$A_d = A_{d0}\left(1 - e^{-\zeta_{\text{ramp}}\tau}\right), \tag{23}$$

where

$$\zeta_{\text{ramp}} = -\frac{\ln(1-0.99)}{8\frac{2\pi}{\omega}},$$

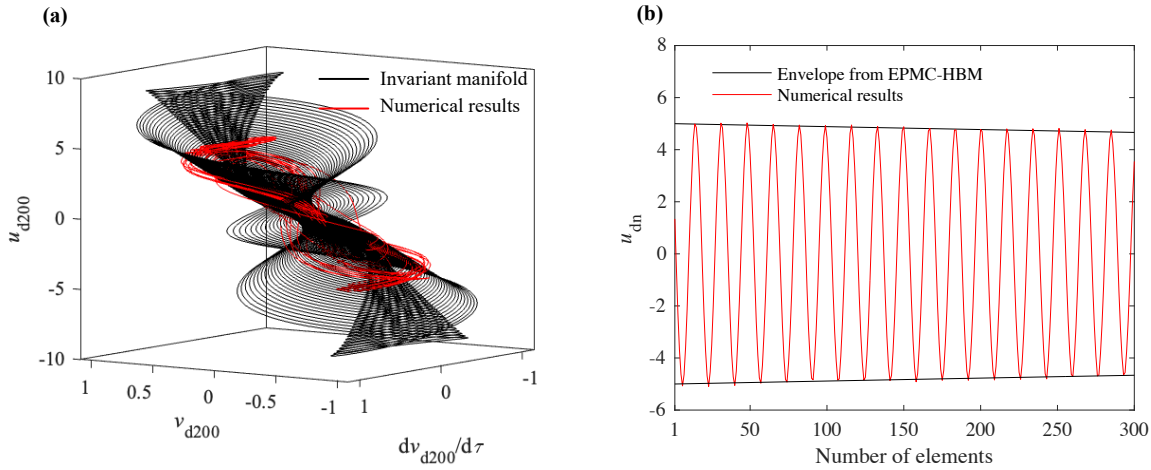

Fig. 4 Underdamped mono-stable metamaterial. Comparison between direct numerical time integration (red line) and numerical results from EPMC-HBM. (a) Reconstruction of the trajectory in space $(v_{d200}, \dot{v}_{d200}, u_{d200})$, highlighting how the direct numerical time history closely follows the curvatures of the invariant manifold obtained from EPMC-HBM. (b) Snapshot of the first 300 elements at $\tau = 500$, with the envelope from EPMC-HBM.

and the peak value A_{d0} is set to 5. In the subsequent analysis, unless otherwise specified, the setting will be used for all the numerical integration computations.

Based on this setting, Fig. 4 highlights the behaviour of the lightly damped wave. In Fig. 4(a), a direct numerical simulation is reconstructed in a pseudo phase space using the displacement and velocities (v_{d200}, $\dot{v}_{d200}$, u_{d200}). It is compared to the invariant manifold obtained from the EPMC-HBM technique, which is constructed by using the extended periodic orbits of the non-conservative system, with the wavenumber selected as $k = 0.38$, which corresponds to $\omega_{de} = 0.355$ in dispersion spectrum. Varying the amplitude along this specific backbone curve, one recovers the invariant manifold associated with this nonlinear wave. It can be observed that the numerical orbit closely follows the curvatures of the invariant manifold, evidencing that the EPMC-HBM technique accurately retrieves the behaviour of the lightly damped metamaterial. Fig. 4(b) presents the snapshot of the first 300 elements of the oscillator chain at time $\tau = 500$, and the envelope of wave attenuation is also provided using Eq. (22). Again, the results illustrate the effectiveness of the predictions given by the present numerical scheme using EPMC-HBM for lightly damped nonlinear dynamics.

4.2 Dispersion properties of conservative metamaterial with internal bistable oscillator

This Section is devoted to analysing the nonlinear dispersion relationships for a metamaterial with bistable nonlinear attachment. Due to the intrinsic two-well dynamics of the bistable oscillator, a wealth of more complex nonlinear behaviours is expected and analysed in this section, which first focuses on the conservative case. The effect of the damping is studied afterwards in Section 4.3.

As mentioned in Section 2, the metamaterial with internal bistable oscillator has three equilibrium points (two stable non-trivial equilibrium points $(u_{dn}, v_{dn}) = (0, \pm E_0)$, and one unstable trivial point $(u_{dn}, v_{dn}) = (0, 0)$), which gives rise to different dispersion branches around the equilibrium points. For the sake of presentation convenience, the acoustic and optic branches near the unstable equilibrium point are referred to as symmetric optic branch (S-OB) and symmetric acoustic branch (S-AB), while those near the stable equilibrium points are called asymmetric acoustic/optical branches (respectively A-AB and A-OB). Note also that the two stable equilibrium points are symmetric to each other, leading to the same spectra. Consequently, when calculating A-AB and A-OB, one only needs to consider the situation at one of the two points, either $(0, E_0)$ or $(0, -E_0)$. In this work, the former is selected.

The parameters of the metamaterial with internal bistable oscillator are the same as those listed in Table 2, except for $l = 0.0501$ m, which implies $l > h$ and $\kappa < 0$. Since conservative dynamics is here studied, the two damping terms, c_m and c_a, are both set to zero. With these settings, the nonlinear dispersion manifold (consisting of backbone curves at different wavenumbers), is then retrieved and shown in Fig. 5(a), highlighting a more complex behaviour as compared to the mono-stable case. In particular, one can observe numerous solution branches in the low-frequency range, for $\omega < 0.7$. To better analyse these nonlinear tongues, a cross-section at a selected amplitude $A_d = 0.1$ is displayed in Fig. 5(b). As in the previous section, by dividing acoustic and optic branches of the dispersion curve by selected integers, one

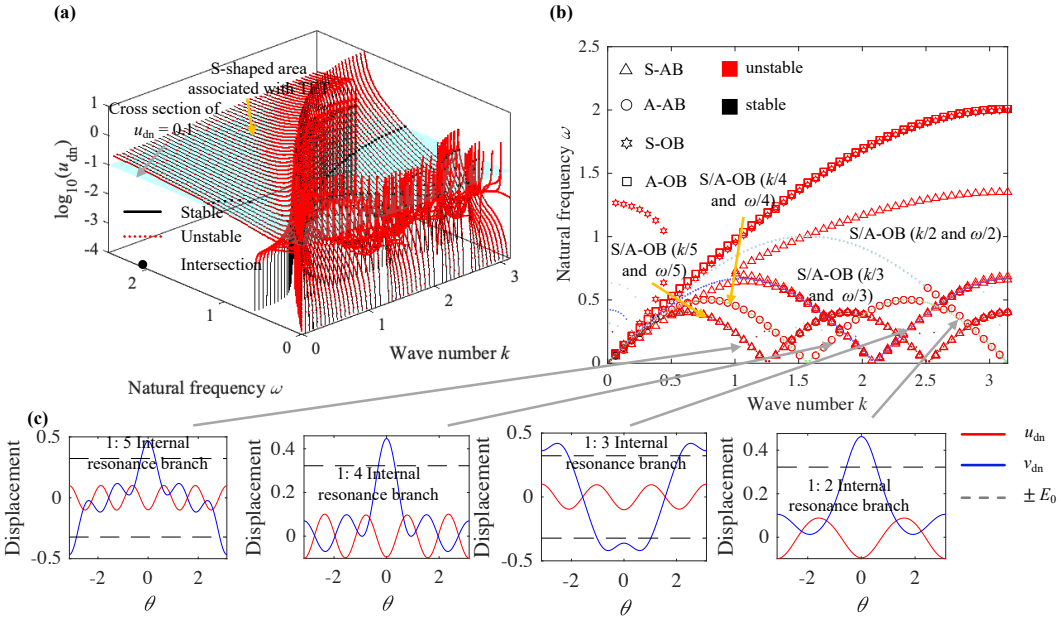

Fig. 5 Dispersion properties and internal resonant waveforms for an undamped metamaterial with internal bistable oscillators. (a) Nonlinear dispersion relationships as a two-dimensional manifold constructed by backbone curves at different wavenumbers. (b) Dispersion spectrum for the selected amplitude $A_d = 0.1$, displaying numerous internal resonance branches. (c) Waveforms in internal resonance branches. In (b), the optic branches where both frequency and wavenumber have been divided by two, three, four and five, are represented with light, dark blue, green, and brown points. The θ in x-axis of (c) denotes the phase angle of harmonic solution Eq. 10, equal to $\omega\tau - ki$, varying from $-\pi$ to π.

can observe a perfect match with the complicated unstable branches, clearly indicating that these dynamical solutions are associated to 1:2/3/4/5 internal resonances between acoustic and optic branches. The even 1:2/4 internal resonant branches originate from A-AB, while the odd internal resonant branches are related to S-AB. Fig. 5(c) also provides the waveforms of these internal resonance branches and displays that the u_{dn} and v_{dn} of 1:3/5 (respectively 1:2/4) internal resonance are symmetric (reps. asymmetric), and exhibit obvious 3rd and 5th (2nd and 4th) harmonic components. They can be presented by using the harmonic solution, Eq.(10). From this equation, one can observe that the wave is a function of both time and space. Thus, varying time and fixing space, or the opposite, or varying both variables are all possible to plot these waveforms. Here, we select a more general presentation, taking the phase angle, $\theta = \omega\tau - ki$ varying from $-\pi$ to π, as x-axis to display internal resonant waves. Another important point to mention is that the internal resonant waveforms presented in Fig. 5(c) and their symmetric counterparts represent the same dispersion solutions. For 1:3/5 internal resonant wave, the two cases denote the same wave, just with a different initial phase. Regarding the remaining 1:2/4 even solutions, the symmetric and original cases correspond to dispersion solutions from equilibrium $(0, -E_0)$ and $(0, E_0)$, exhibiting identical dynamic behaviours. Therefore, only one of the two cases is plotted in Fig. 5(c). Returning these rich internal resonant branches, they could trigger chaotic inter-well motion, aiding the metamaterial with numerous internal bistable oscillators in achieving excellent wave attenuation performance at low wave amplitudes. In Fig. 5(a), there is also an unstable S-shaped region in S-OB, which is realized by the bending of the backbone curve of S-OB. The region can also be observed in mono-stable nonlinear metastructure, see Fig. 3(a). In the following discussion about wave attenuation, it will be proven that such S-shaped area is responsible for the targeted energy transfer (TET) mechanism, and is helpful to improve the wave attenuation.

The dispersion manifold shown in Fig. 5(a) exhibits complex stability variation, internal resonance, and bifurcation behaviours as the wave amplitude increases. Let us more deeply investigate the different solutions obtained for increasing amplitudes, by selecting 4 different levels: $A_d = 1 \times 10^{-4}$, 0.05, 0.5, and 5. Fig. 6 analyses the obtained results while Figs. 7 - 9 give more insights into the obtained dynamics by displaying numerical integration and wavelet transform to examine the solutions.

4.2.1 small wave amplitude: $A_d = 1 \times 10^{-4}$

For small wave amplitude $A_d = 1 \times 10^{-4}$, the dispersion spectrum is presented in Fig. 6(a). The symmetric acoustic and optic branches S-AB and S-OB are unstable, while the asymmetric ones, A-AB and A-OB, remain stable. The instability in S-A/OB is associated with internal resonance and the unstable trivial

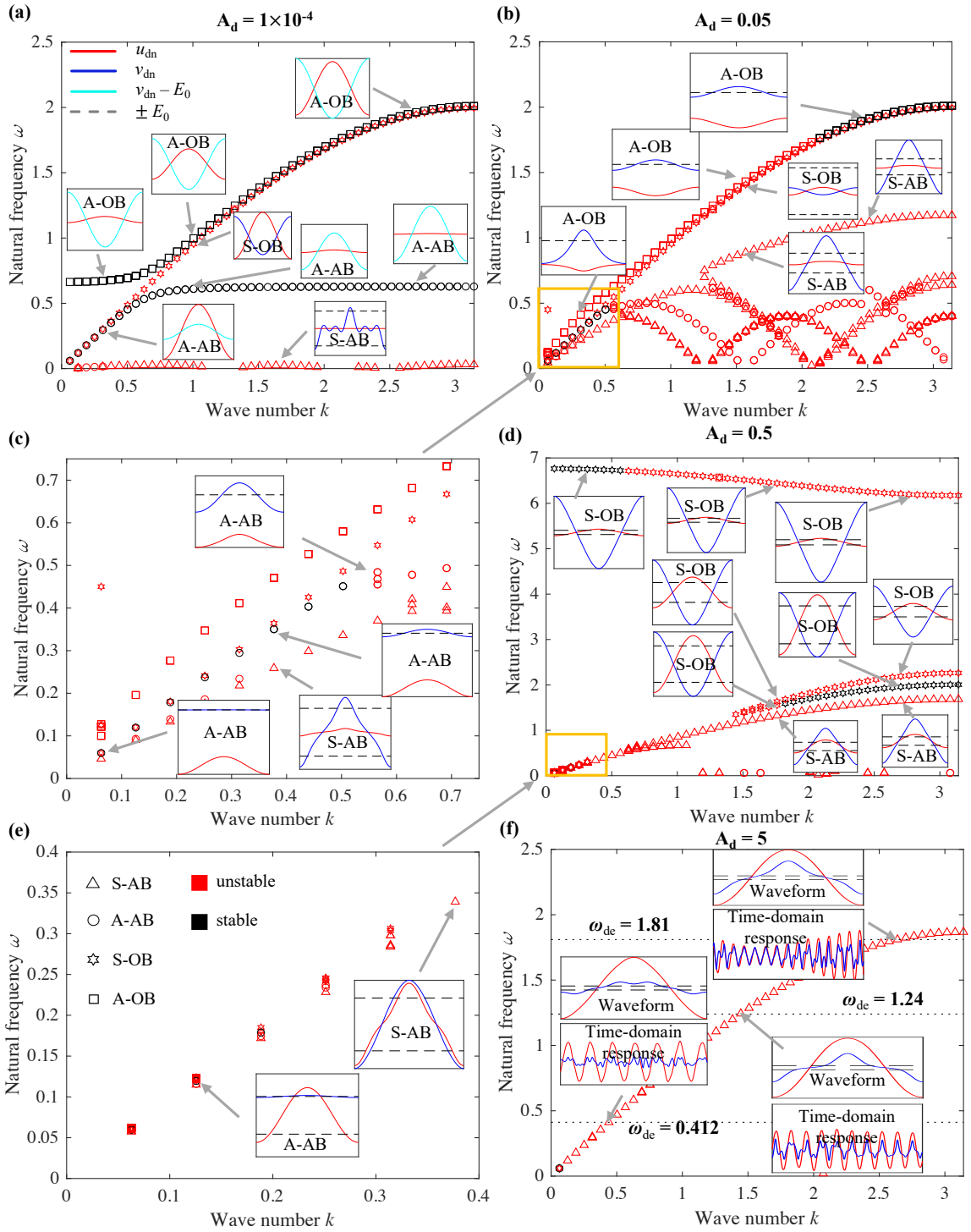

Fig. 6 Dispersion spectrum and corresponding waveforms of undamped metamaterial with internal bistable oscillator at (a) $A_d = 1 \times 10^{-4}$, (b) 0.05, (c) Zoom of (b), (d) $A_d = 0.5$, (e) Zoom of (d), (f) $A_d = 5$. The definitions of x and y-coordinates of the inserted figures displaying waveforms are the same as in Fig. 5(c), with the x-axis representing the phase angle θ, and the y-axis the dimensionless displacement. The time-domain responses in (f) come from the numerical integration of finite oscillator chains, and their x and y-coordinates denote the time τ and displacement of the 20th cell.

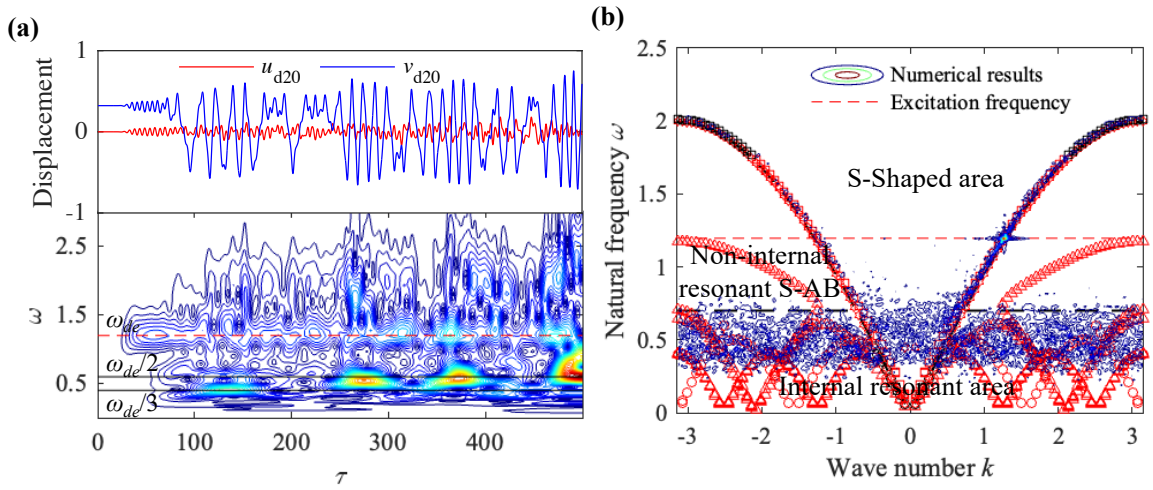

Fig. 7 Numerical response of the undamped matematerial with internal bistable oscillator under input waves with $A_d = 0.05$ and $\omega_{de} = 1.2$. (a) Time-domain response and time-frequency diagram of the 20th element, (b) 2D Fourier spectrum of 10 – 450th elements superimposed to the dispersion solution branches

.

equilibrium point, which makes the associated waves unsustainable in practice. If these symmetric branches are neglected, the dispersion properties of the metamaterial with internal bistable attachment at low amplitudes are controlled by A-A/OB and with a bandgap in $0.63 < \omega < 0.68$. For a better understanding, the waveforms of A-A/OB are provided in the inserted figures. In some cases and to improve readability, a static shift has been employed to align the v_{dn} wave in asymmetric branches with the zero axis. In these cases, the shift is E_0 and another light blue is used to refer to these shifted waves. Note also that in these inserts, the x-axis is θ, as already used in Fig. 5. From these waveforms, it is observed that along the A-AB branch, u_{dn} and v_{dn} move in phase, and v_{dn} increases with the wavenumber, indicating a concentration effect of wave energy into the bistable oscillator. Whereas for A-OB, the opposite is true, i.e., u_{dn} and v_{dn} move in out-phase and v_{dn} decreases as the wavenumber increases.

4.2.2 Moderate amplitude: $A_d = 0.05$

When A_d reaches 0.05, the dispersion spectrum becomes complex, as highlighted in Figs. 6(b) and (c). Apart from unstable S-A/OB branches, there also occurs some unstable tongues, which are separated from S/A-AB at $\omega < 0.7$, and associated with 1:2/3/4/5 internal resonance. In the non-internally resonant regions ($k < 0.6$ or $\omega > 0.7$), the displacements u_{dn} and v_{dn} along the symmetric acoustic branch S-AB move symmetrically in phase, with v_{dn} crossing the stable equilibrium points E_0. As for S-OB, its u_{dn} and v_{dn} still display out-of-phase motion around the zero point. For the asymmetric branches, A-AB remains stable in the low wavenumber region $k < 0.5$, with u_{dn} and v_{dn} moving in phase. As the wavenumber k increases, the amplitude of v_{dn} significantly rises, see Fig. 6(c). As for A-OB, its waveforms show asymmetric an out-of-phase motion, with larger v_{dn} at smaller wavenumbers. It is unstable at low wavenumbers but stable for high wavenumbers.

In the range $0.5 < \omega < 1.6$, there is no longer bandgap for larger wave amplitude, $A_d = 0.05$, only unstable dispersion branches in Fig. 6(b). To provide some sense for the potential responses within this region, Fig. 7 presents the numerical responses of the system at $\omega_{de} = 1.2$. The time-domain and time-frequency results shown in Fig. 7(a) highlight that the chaotic inter-well motion is excited via 1:2/3 internal resonances, which is thus the awaited dynamical solution when one inputs a wave in this unstable frequency region. The chaotic response may be related to the rich resonant behaviour due to the presence of the numerous branches in S/A-AB. This is confirmed by the numerical results shown in Fig. 7(b), where the 2D Fourier spectrum is superimposed to the dispersion curves, underlining that the system response is mainly concentrated in the internal resonant area.

Fig. 8 uses both EPMC-HBM and numerical integration techniques to present the phase diagrams for the 20th element at ω_{de}=1.2 and 1.95, to shed light on the nature of the dynamical solutions obtained with regard to the location of the stable/unstable points of the bistable oscillator. Additionally, the homoclinic orbits of the unstable fixed point at the origin, are also reported, since these particular orbits can be used

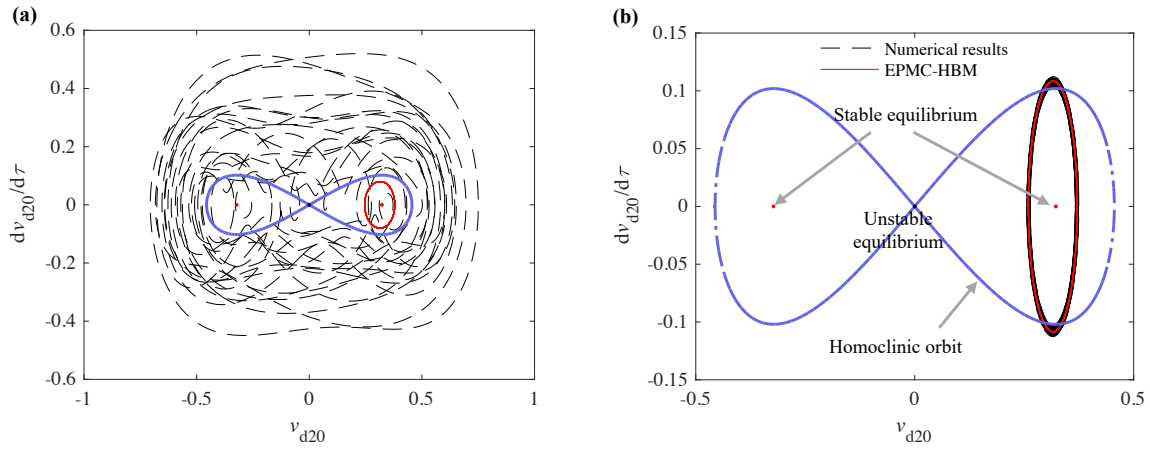

Fig. 8 Phase space representation of 20th element along the A-OB branch with an input wave amplitude $A_d = 0.05$. (a) excitation frequency $\omega_{de} = 1.20$. The periodic orbit (red line) given by EPMC-HBM is unstable such that a chaotic inter-well motion settles down. (b) excitation frequency $\omega_{de} = 1.95$. The periodic orbit is stable and the direct numerical integration retrieves this solution. Blue curves: homoclinic orbits of the saddle point.

as pseudo-separatrix to distinguish the different solutions as intra- or inter-well dynamics, see *e.g.* [30, 33]. The homoclinic orbits can be directly derived by vanishing the Hamiltonian of the internal bistable attachment [30], *i.e.* by solving $H(\dot{v}_{dn}, v_{dn}) = \dot{v}_{dn}^2/2 + \kappa v_{dn}^2/2 + \gamma v_{dn}^4/4 = 0$.

The numerical results given in Fig. 6(b) show that the low-frequency intra-well motion predicted by EPMC-HBM is unstable for ω_{de}=1.2, while it is stable for ω_{de}=1.95. Consequently, in Fig. 8(a), the periodic orbit (red line) predicted by the continuation method cannot be retrieved by a time simulation. Instead, a chaotic inter-well motion setlles down, showing large amplitude oscillations as compared to the amplitude of the homoclinic orbits. On the other hand, for ω_{de}=1.95, a periodic intra-well motion with large amplitude settles down, which explains the stable branch observed for this particular amplitude in Fig. 7(b).

4.2.3 Moderately large amplitude: $A_d = 0.5$

The moderately large wave amplitude is now investigated with $A_d = 0.5$, and reported in Figs. 6(d) and (e). In that case, the wave amplitude has already exceeded E_0. Therefore, the asymmetric branches have almost disappeared, leaving only a small portion of stable A-AB branch with very small displacement v_{dn} in the low wavenumber region. For S-AB, the entire branch is unstable, and most tongues have disappeared, leaving only a 1:3 internal resonant branch near $0.7 < \omega < 1.1$. For the non-internal resonant part, u_{dn} and v_{dn} of S-AB show in-phase motion, and as the wavenumber increases, the vibrational energy concentrates towards the bistable oscillator. As for S-OB, it has three segments, which are related to the S-shaped area in Fig. 5(a). These three segments correspond to the areas before the first extremum, between the first and second extrema, and after the second extremum of the backbone curve. Observing the waveforms of these branches, it can be seen that u_{dn} and v_{dn} on S-OB are in an out-of-phase motion. And at the same wavenumber, the higher the frequency implies the larger the amplitude v_{dn}. That indicates that the high-frequency S-shaped region has an excellent ability to transfer the main chain's energy into the nonlinear attachments.

For this case without internal resonance branches, the possible response, in the unstable frequency range $0.2 < \omega < 1.5$, is investigated in Fig. 9 by setting $\omega_{de} = 1.07$. Figures 9(a) and (b) show that a chaotic response is triggered in the 20th element, where the displacements u_{d20} and v_{d20} alternate to perform symmetric in-phase and out-of-phase motion, and its two-dimensional Fourier spectrum is concentrated in the non-resonant S-AB and the S-shaped region of S-OB. This unstable response results from the coupling between the two dispersion branches. For the underdamped case, such coupling effect can also trigger TET to accelerate wave attenuation, which will be presented in the following Sec. 4.3.

4.2.4 large amplitude: $A_d = 5$

When A_d reaches 5, almost all solutions are unstable within $0 < \omega < 2.5$, see Fig. 6(f). The S-OB branch outside this range or plot have very high frequencies, $\omega > 40$, and significant v_{dn} in their waveforms, making them difficult to excite in practice, so they do not need to be discussed. Turning our attention back to the

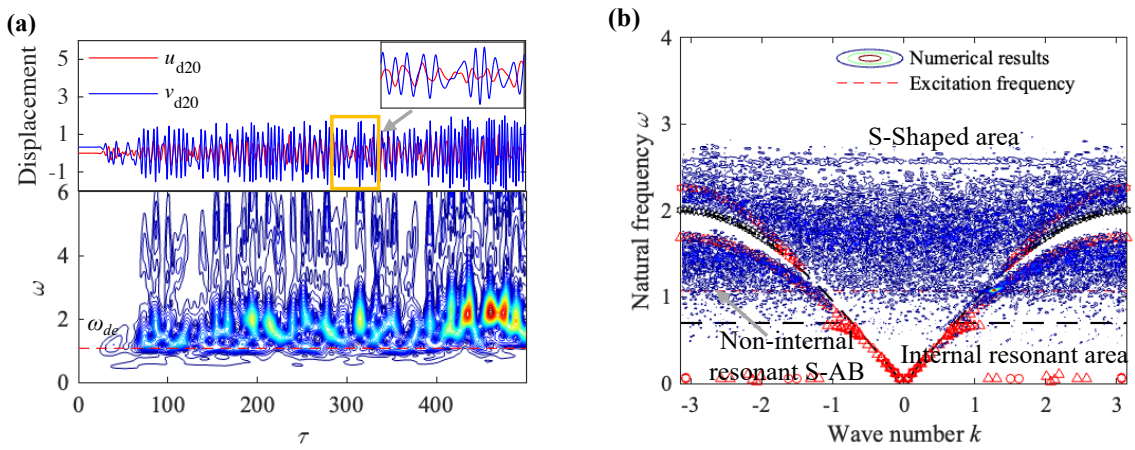

Fig. 9 Numerical response of the undamped metamaterial with internal bistable attachments, under input waves with $A_d = 0.5$ and $\omega_{de} = 1.07$. (a) Time-domain response and time-frequency diagram of 20th element, (b) Two-dimensional Fourier spectrum of 10 – 450th elements, superimposed to the dispersion solution branches.

acoustic branches, A-AB appears only in a very low wavenumber range. For S-AB, u_{dn} and v_{dn} also move in phase, but v_{dn} has clear high harmonic components. As the wavenumber increases, the influence of high harmonic components gradually weakens, but the amplitude of v_{dn} progressively increases and approaches u_{dn}. Another point to note is that S-AB is globally unstable, but numerical integration results at $\omega_{de} =$ 0.412, 1.24, and 1.81 with $A_d = 5$ show that the time-domain responses are still resembling the waveforms of the unstable periodic orbits. This suggests that the dispersion spectrum of S-AB can qualitatively assess these unstable responses. In fact, such a phenomenon results from extremely large amplitude oscillations, which makes the bistable oscillator far away from the two potential wells, behaving like an attachment to a rigid connection. That prevents the appearance of chaotic inter-well motion and coupling motion between S-AB and S-OB.

As a summary of all the findings obtained thanks to the numerical simulations shown in this Section, it can be concluded that at small wave amplitudes, the metamaterial with internal bistable oscillator behaves like a linear structure, exhibiting stable A-A/OB and with resonant bandgap. However, as the wave amplitude increases, the bandgap disappears, and the unstable dispersion solutions emerge over a broader frequency range. These solutions may trigger chaotic inter-well motions related to sub-harmonic internal resonance and unstable responses associated with the coupling between non-internal resonant S-AB and S-shaped regions in S-OB. At very high wave amplitudes, the unstable S-AB dominates the entire frequency range (ignoring A-AB, which is almost unexcitable). Although S-AB is unstable, it can still assess wave propagation.

4.3 Wave attenuation of the metamaterial with internal bistable oscillators

4.3.1 Damped attenuation coefficients under varying wave amplitudes

In this Section, a general overview of the dissipative characteristics of lightly damped metamaterial with bistable attachments is given, thanks to the scalar measurement of the wave attenuation provided by the EPMC. The model parameters used for the numerical simulations are the same as in Sec. 4.2, except for c_m = 0.01 N·s/m, $c_a = 0.02$ N·s/m. Based on these settings, figure 10 first presents the attenuation coefficients $\zeta\omega$ at different wave amplitudes $A_d = 1\times10^{-4}$, 0.05, 0.5, 5. For $A_d = 1\times10^{-4}$, see Fig. 10(a), the symmetric branches are both unstable, where S-AB occurs at very low frequencies and has a lot of energy within the v_{dn}, while S-OB behaves like a saddle, so they are unlikely to be excited in practice and not elaborated upon here. Regarding asymmetric solutions, the A-AB shows a very low attenuation coefficient in the low wavenumber region, but as the wavenumber increases, so does the attenuation coefficient. Especially as the frequency approaches the bandgap, the attenuation coefficient of A-AB rapidly increases to about 0.03. A-OB also has a high attenuation coefficient near the bandgap, but its relationship with wavenumber is the opposite of A-AB. In short, the solution near bandgap, whether for A-AB or OB, has the best attenuation effect.

When $A_d = 0.05$, the dispersion curve exhibits numerous high damping internal resonant branches, as shown in Fig. 10(b). Their damped attenuation coefficients $\zeta\omega$ reach values up to 0.03, close to the best results obtained in the previous case near bandgap. This implies that the chaotic motion associated with

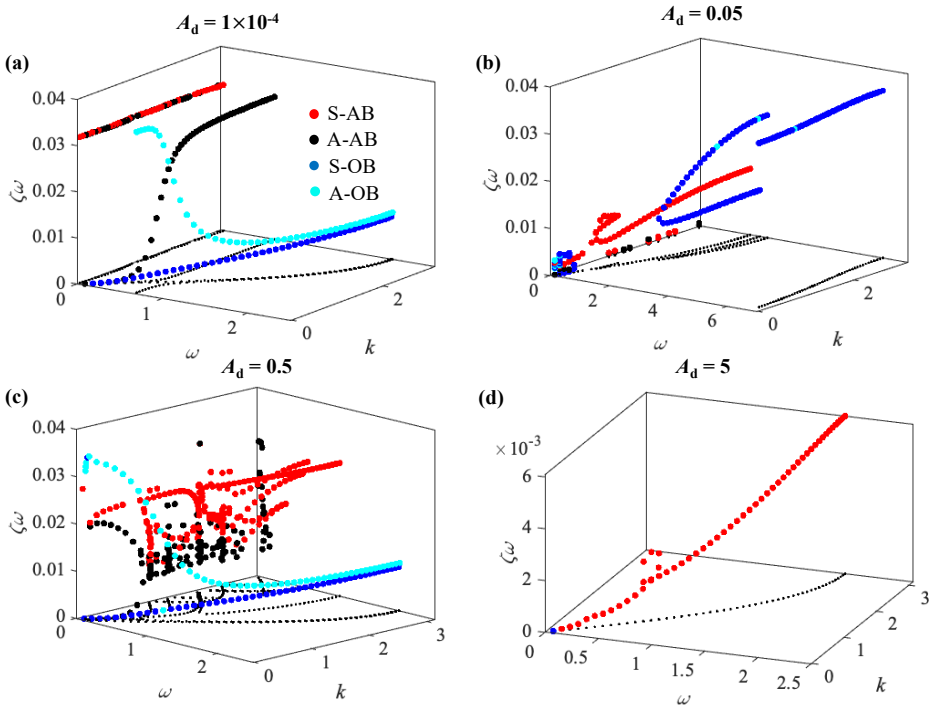

Fig. 10 Damped attenuation coefficients $\zeta\omega$ of different dispersion branches for damped multi-stable metamaterial at A_d = (a) 1×10^{-4}, (b) 0.05, (c) 0.5, and (d) 5

these internal resonant branches has the ability of fast dissipation of the wave energy. As for A-AB, it still shows minimal attenuation coefficients in the low wavenumber region, almost lacking wave attenuation capability.

As A_d reaches 0.5, see Fig. 10(c), internal resonant branches and A-OB disappear. A-AB only appears in a very low wavenumber region with weak wave attenuation performance. The attenuation coefficient of S-AB increases with wavenumber, up to 0.017. The S-OB is divided into three segments, where branches with higher frequencies at the same wavenumber exhibit a better damping performance. These high-damping branches belong to the S-shaped region of S-OB. When $A_d = 5$, see Fig. 10(d), only acoustic branches exist in the range $0 < \omega < 2.5$. The attenuation coefficients of S-AB are much smaller than those in Fig. 10(c), with a maximum of only 6×10^{-3}. This indicates that an increase in wave amplitude weakens the wave attenuation performance of S-AB.

From the above four cases, it can be concluded that the best-case scenarios in terms of attenuation capabilities, are obtained either when a chaotic inter-well motion is excited, near bandgap where the periodic solutions are unstable, or in the S-shaped area where nonlinear branches are related to the internal resonant solution. These cases lead to optimal performance in wave energy dissipation, however, it requires a suitable frequency and amplitude tuning. More insights are now given to these typical solutions by closely inspecting the different dynamical characteristics, for different amplitudes and excitation frequencies corresponding to the interesting cases found.

4.3.2 Wave attenuation for varying amplitudes and frequencies

For the four wave amplitudes that have been selected and studied before, the influence of frequency on wave attenuation is discussed in detail in Figs. 11-15. Figure 11 starts by setting $A_d = 1 \times 10^{-4}$ and $\omega_{de} = 0.237$, 0.534, 0.803 and 1.82. While $\omega_{de} = 0.237$ and 0.534 intersect with A-AB, $\omega_{de} = 0.534$ and 0.803 are related to A-OB, see Fig. 11(a). For the lowest $\omega_{de} = 0.237$, Fig. 11(b), the input wave decays very slowly due to the low-damping waveform of A-AB. The attenuation rate for higher $\omega_{de} = 0.534$ is much faster, benefiting from the significant increase of the attenuation coefficient in A-AB near bandgap. As for A-OB, although the low-frequency attenuation coefficient is larger than the high-frequency one, the snapshots in Fig. 11(d) and (e) show that the attenuation rates in both cases are not significantly different. This might be because the group velocity of A-OB is lower at high frequencies, requiring more time for the wave to travel the same distance in the lattice. The envelopes of u_{dn} based on Eq. (22) are also plotted in Figs. 11(b–e), well matching the numerical integration results, further validating the EPMC-HBM.

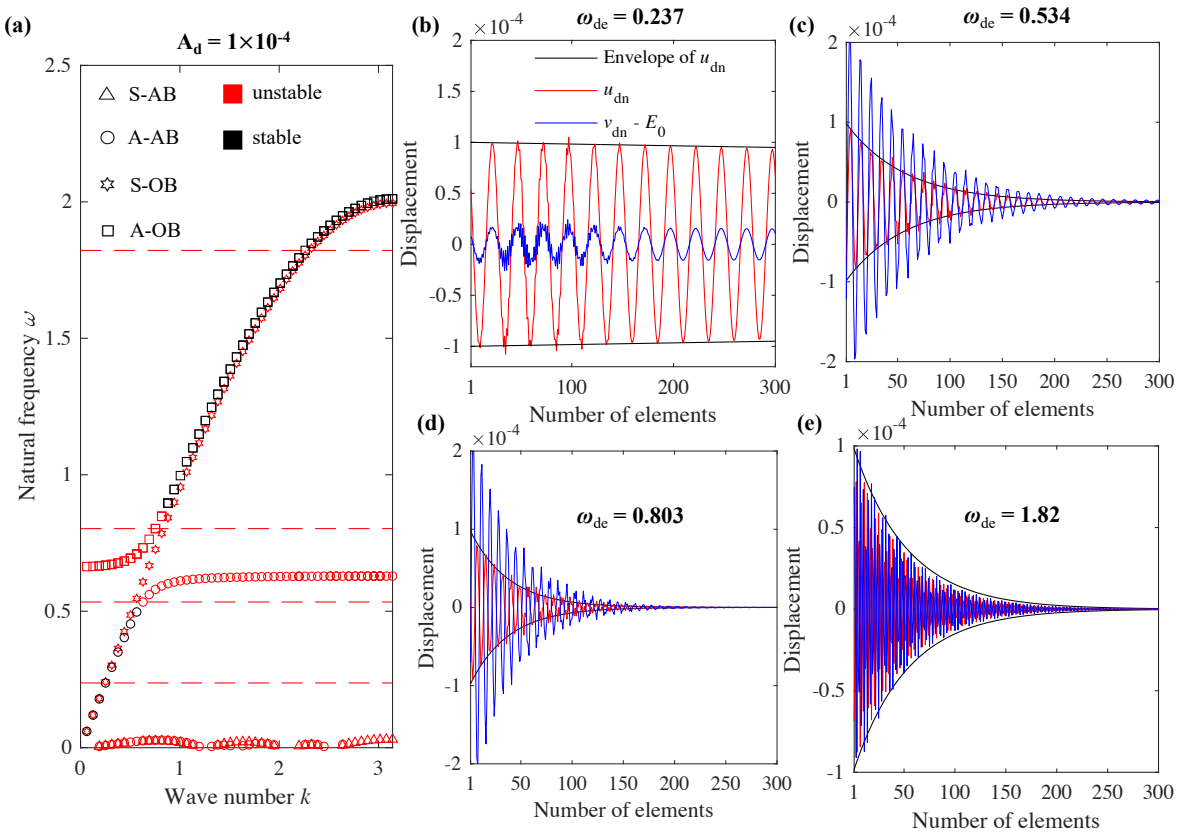

Fig. 11 Wave attenuation in lightly damped bi-stable metamaterial when $A_d = 1 \times 10^{-4}$. (a) Dispersion spectrum. (b-e) Spatial representation of the wave along the lattice for different excitation frequencies at time $\tau = 500$. Comparison between the envelope obtained from EPMC-HBM (black line) and direct numerical simulation (red: u_{dn}, blue: $v_{dn} - E_0$). Excitation frequencies ω_{de} marked by dashed red lines in (a) selected as: (b) 0.237, (c) 0.534, (d) 0.803 and (e) 1.82.

For the amplitude of input wave as $A_d = 0.05$, four different excitation frequencies, $\omega_{de} = 0.179$, 0.403, 0.992, and 1.89, are illustrated in Fig. 12. The first two frequencies intersect with the stable A-AB. Their results in Fig. 12(b) and (c) show that the lower the frequency implies the slower the wave attenuation rate. As for the other two excitation frequencies, they fall within the unstable and stable regions of A-OB, respectively. In the unstable region with $\omega_{de} = 0.992$, a chaotic inter-well motion is obtained, but is observable only for the left-hand side of the lattice where energy is input, as shown in Fig. 12(d). After that, the wave, with a half-wavenumber component, continues to decay until the 75th element, finally dissipating energy according to the waveform of A-OB. From the space-wavenumber spectrum in Fig. 12(d), another interesting result is obtained. The wavenumber does not undergo significant changes in the wave attenuation process without internal resonance. This aligns with the form of Eq. (22), its wavenumber is independent of the time variable and wave amplitude. This implies the invariance of the wavenumber when the amplitude varies. It's worth noting that such a conclusion is limited to metamaterials with invariant lattice parameters, which is fundamental for employing the Bloch's theorem to derive Eq. (22). Appendix B also provides examples further illustrating this phenomenon. For $\omega_{de} = 1.89$, see Fig. 12(e), input wave decays according to the stable waveform of A-OB and demonstrates the best damping performance, which is the consequence of the slow group velocity in the high-frequency range of A-OB.

The wave attenuation process at $A_d = 0.5$ for $\omega_{de} = 0.179$, 0.393, 1.42, and 1.89 is analysed in Fig. 13. Among these four frequencies, the smallest, $\omega_{de} = 0.179$, intersects with the stable branch of A-AB, where the input wave follows its slow dynamic equation resulting in an extremely slow attenuation, as shown in Fig. 13(b). For a larger $\omega_{de} = 0.393$, which connects with unstable S-AB, the attenuation process can be divided into two stages, as shown in Fig. 13(c). In the first one, the displacements u_{dn} and v_{dn} decay according to S-AB covering elements 1-100. Then, wave attenuation is accelerated via TET at the end of the first stage. After TET, the waveform becomes asymmetric with an out-of-phase motion in A-AB. Due to the very low attenuation coefficient of A-AB, the remaining wave energy hardly attenuates in the second stage. Observing this attenuation process, it appears that the unstable S-AB does not produce chaotic inter-well motion during wave attenuation. This might be because the excited waveform is located at $k = 0.5$, where no

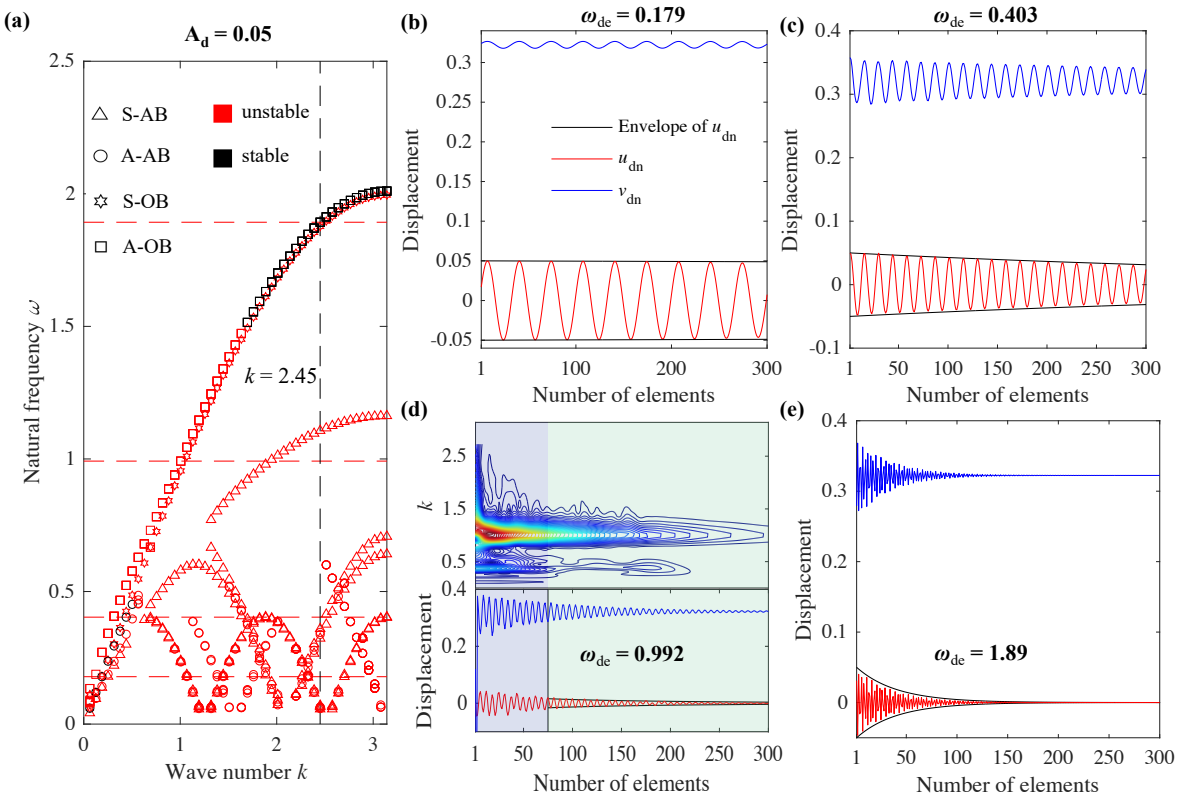

Fig. 12 Wave attenuation in lightly damped bi-stable metamaterial when $A_d = 0.05$. (a) Dispersion spectrum. (b-e) Spatial representation of the wave along the lattice for different excitation frequencies at time $\tau = 500$ (1000 for (e)). Comparison between the envelope obtained from EPMC-HBM (black line) and direct numerical simulation (red: u_{dn}, blue: v_{dn}). Excitation frequencies ω_{de} marked by dashed red lines in (a) selected as: (b) 0.179, (c) 0.403, (d) 0.992 and (e) 1.89. In (d), the space-wavenumber spectrum diagram is superimposed.

internal resonant branches are nearby. For $\omega_{de} = 1.42$, this issue does not arise, the chaotic inter-well motion is triggered at the beginning, and the u_{dn} is quickly reduced to a relatively low level, as shown in Fig. 13(d). In the region of chaotic inter-well motion, the wavenumber components of response are dispersed across the entire first Brillouin zone, with high wavenumber components having higher attenuation coefficients and being quickly dissipated. Thus, only low wavenumber and low damping components of A-AB are retained for propagation after the 150th elements. For $\omega_{de} = 1.89$, the snapshot in Fig. 13(e) is also quite interesting. Since high-frequency S-OB and A-OB are both stable, see Figs. 12 and 13 (a), the input wave demonstrates a smooth transition from a symmetric waveform in S-OB to the asymmetric waveform of A-OB when wave amplitude attenuates to a certain extent. Throughout the attenuation process, the response's wavenumber remains unchanged, and the slow dynamic equations of S-OB and A-OB can accurately predict the envelope of u_{dn}. This particular feature is further illustrated in Fig. 14, where the invariant manifolds of S-OB and A-OB at k=2.45 obtained from EPMC-HBM are superimposed to the time-domain response of the 20th element in a reconstructed phase space $(v_{d20}, \dot{v}_{d20}, u_{d20})$, the selected value k=2.45 corresponds to $\omega_{de} = 1.89$ for numerical integration in Figs. 12 and 13 (a). As time passes, the trajectory of $(v_{d20}, \dot{v}_{d20}, u_{d20})$ starts from the initial point $(E_0, 0, 0)$ and increases along the surface of A-OB. When the amplitude reaches certain values, it switches to the S-OB and finally ends on this surface.

To investigate wave propagation behaviour at large wave amplitude $A_d = 5$, $\omega_{de} = 0.178$, 0.639, 1.12, and 1.76 are set to perform numerical analysis. Figure 15 shows that the four selected frequencies fall in the unstable S-AB branch. Due to this instability, their waves also do not strictly decay according to the slow dynamic equations. For the lower frequency wave, the coincidence with the predicted envelope is still good, while in the other three cases, only the overall trend can be evaluated. Figures 15(b - e) demonstrate that the higher the frequency, the faster the wave attenuation rate. This is caused by the larger damping value and the slower group velocity encountered along the high-frequency S-AB branch. The wave at $\omega_{de} = 1.12$ decays according to the waveform of S-AB in the first 250 elements and then triggers TET, see Fig. 15(d). For $\omega_{de} = 1.76$, the wave decays according to S-AB in the first 60 elements, then triggers chaotic inter-well motion to dissipate energy, and finally switches to the waveform of A-AB to continue propagation, as shown in Fig. 15(e).

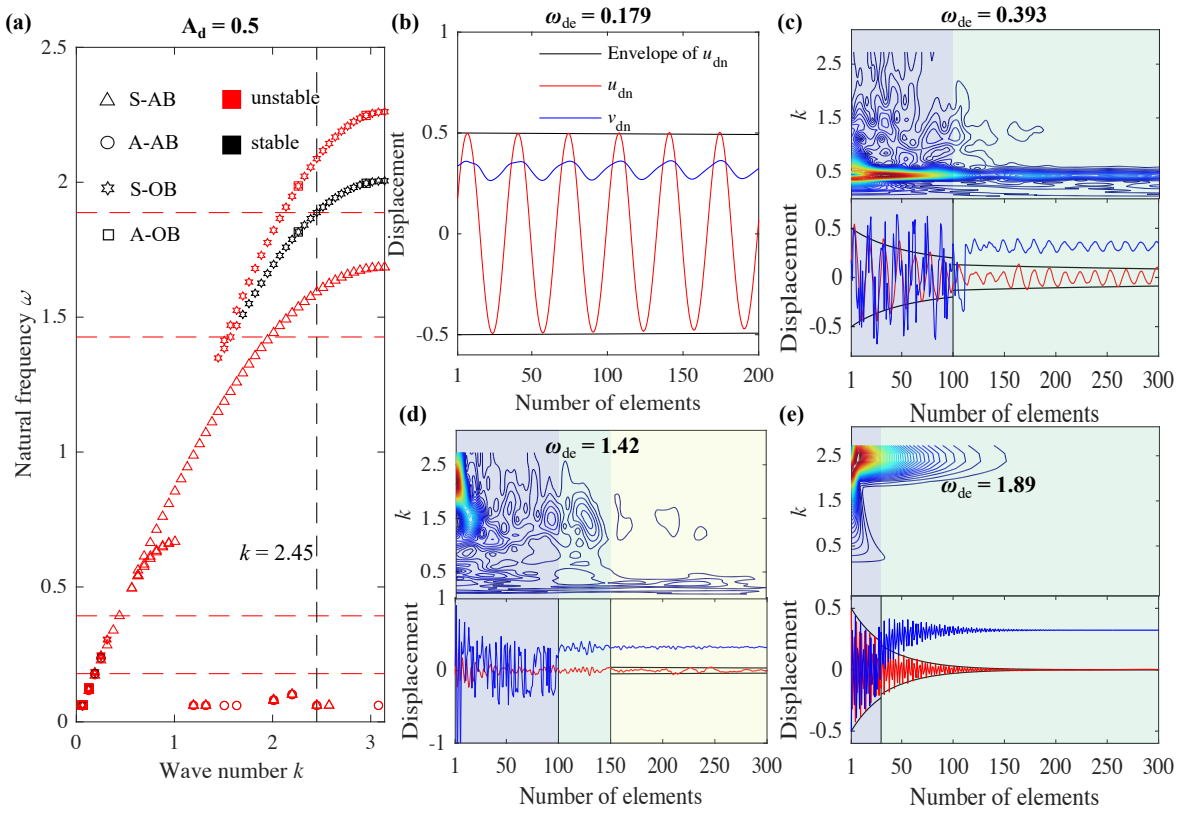

Fig. 13 Wave attenuation in lightly damped bi-stable metamaterial when $A_d = 0.5$. (a) Dispersion spectrum. (b-e) Spatial representation of the wave along the lattice for different excitation frequencies at time $\tau = 500$. Comparison between the envelope obtained from EPMC-HBM (black line) and direct numerical simulation (red: u_{dn}, blue: v_{dn}). Excitation frequencies ω_{de} marked by dashed red lines in (a) selected as: (b) 0.179, (c) 0.393, (d) 1.42 and (e) 1.89. In (c-e), the space-wavenumber spectrum diagram is superimposed.

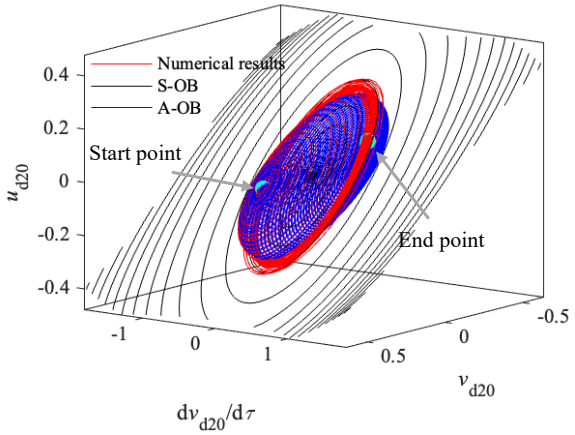

Fig. 14 Trajectory from a direct time integration with $A_d = 0.5$ and $\omega_{de} = 1.89$ superimposed with the invariant manifolds computed from EPMC-HBM, respectively for the S-AB branch in black and the A-0B branch in blue, for k=2.45 (which corresponds to $\omega_{de} = 1.89$ in Fig. 13(a)). The light blue points denote the starting and ending points of the numerical trajectory, where the initial condition is $(v_{d20}, \dot{v}_{d20}, u_{d20}) = (E_0, 0, 0)$. This representation in a 3d view of the phase space shows how this particular trajectory transitions from one invariant manifold to the other.

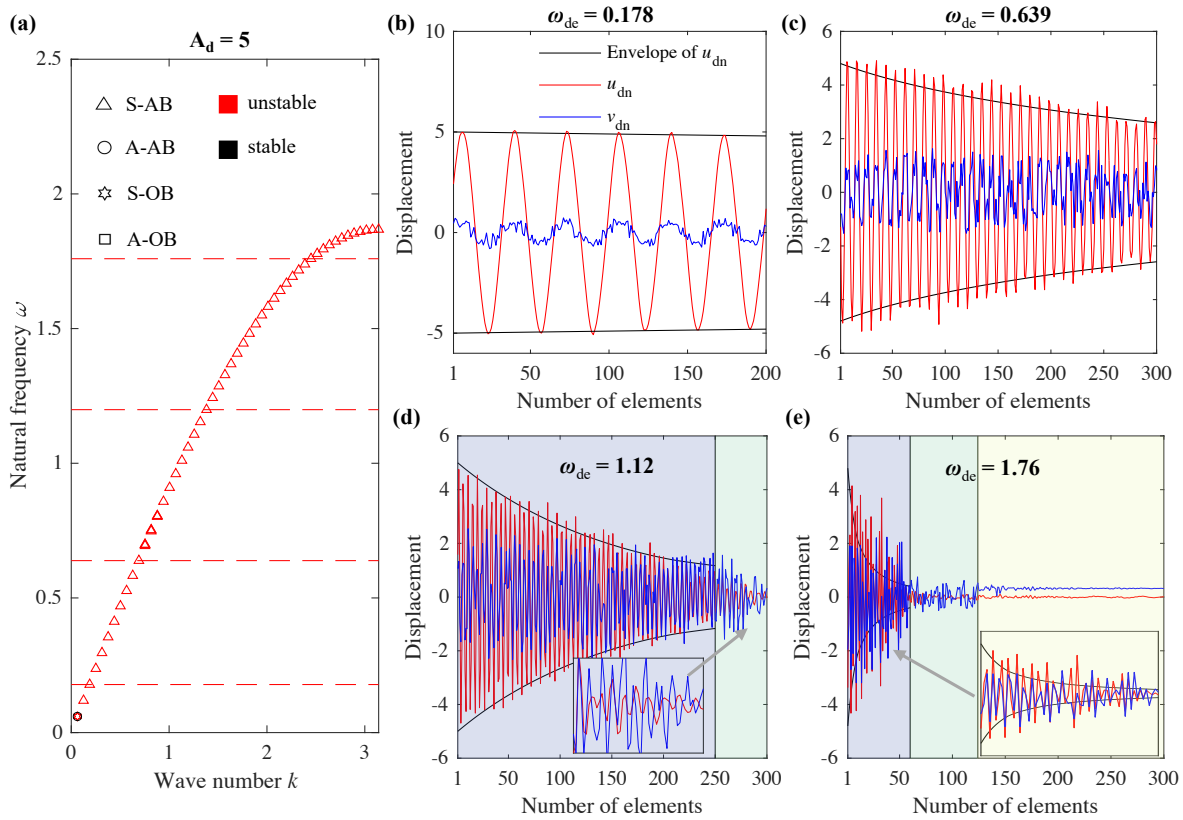

Fig. 15 Wave attenuation in lightly damped bi-stable metamaterial when $A_d = 5$. (a) Dispersion spectrum. (b-e) Spatial representation of the wave along the lattice for different excitation frequencies at time $\tau = 500$ (1000 for (e)). Comparison between the envelope obtained from EPMC-HBM (black line) and direct numerical simulation (red: u_{dn}, blue: v_{dn}). Excitation frequencies ω_{de} marked by dashed red lines in (a) selected as: (b) 0.178, (c) 0.639, (d) 1.12, and (e) 1.76.

5 Conclusion

This paper is devoted to the analysis of the nonlinear dispersion relationships of metamaterials embedding bistable oscillators. In order to achieve a complete picture including both conservative and dissipative characteristics, strongly nonlinear regimes and internal resonances, a numerical technique combining EPMC, HBM and numerical continuation, has been used. The technique is not only effective for analysing the evolution of dispersion properties and discussing the impact of damping on wave propagation but is also able to address internal resonances in metamaterials — a challenge that previous nonlinear analysis techniques based on Bloch's assumption could not figure out.

In the conservative case, multi-stable metamaterials exhibit more complex dispersion properties as compared to the mono-stable ones. The two-degrees-of-freedom bistable lattice has multiple distinct equilibrium points, each with acoustic and optic dispersion branches. Thus, there are asymmetric and symmetric acoustic/optical branches (respectively denoted as A-A/OB and S-A/OB) related to stable and unstable equilibrium points, respectively, with waveforms exhibiting asymmetric and symmetric in-phase/out-of-phase motions. The S/A-AB branches contain numerous tongues, which are 1:2/3/4/5 internally resonant branches between acoustic and optical branches, where lower ratio internal resonances (1:2/3) may trigger chaotic inter-well motion. Interestingly, at higher frequencies, the backbone curves of S-OB develop an unstable S-shaped region. Thanks to this specific feature, targeted energy transfer can take place for these parameters, which will ultimately lead to enhanced attenuation properties when damping is taken into account. Among all the found features, the characteristics of multi-dispersion branches and multi-internal resonance branches are unique to the multi-stable metamaterial, which is also the main reason for its excellent wave manipulation and attenuation ability.

The wave attenuation performance of damped metamaterial with internal bistable oscillators is influenced by wave amplitude and frequency. For small amplitudes, symmetric dispersion branches are unlikely to be excited, and asymmetric branches are controlled by the linearized model near the stable equilibrium point, featuring a locally resonant bandgap. A-A/OB near the bandgap exhibits significant wave attenuation

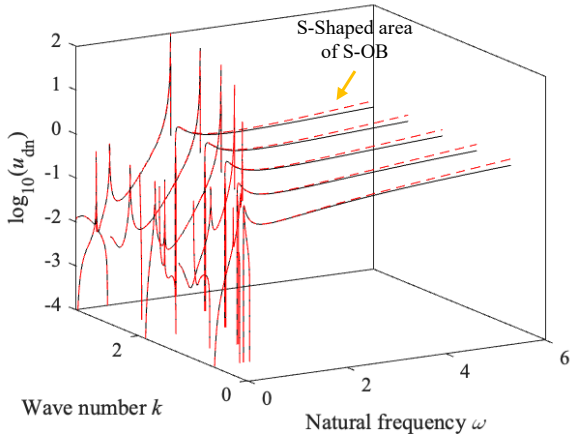

Fig. A-1 Comparison of exact and approximate third-order models in predicting the backbone curves for five different wavenumbers $k = i\pi/5, i = 1, 2, \cdots, 5$.

performance. High-frequency A-OB has a small group velocity, making it difficult for waves to propagate through the damped oscillator chain. The low-frequency A-AB branch has poor damping performance, allowing waves to propagate with an almost constant amplitude over long distances. Notably, the poor performance in A-AB is regardless of wave amplitude. As wave amplitude increases, the bandgap gradually disappears, but unstable A-OB and S-AB remain over a broader frequency range. When the input wave frequency falls within this range, it may trigger high-damping chaotic inter-well motion and targeted energy transfer. The low and high-frequency ranges are governed by stable A-AB and A/S-OB, respectively. At very high amplitudes, only waves of S-AB can propagate through the metamaterial, with its damping performance affected by wavenumber and amplitude, the smaller the wavenumber and the larger the amplitude, the poorer wave attenuation performance. In these cases, the emergence of chaotic inter-well motion and targeted energy transfer at moderate amplitudes usually result in the best and robust wave attenuation over a wide frequency band. However, achieving great damping performance for multi-stable metamaterial within a specified wave amplitude range also requires careful design of bistable attachments, which will be the focus of a future work.

As a last remark, it is found that the wavenumber remains unchanged during wave attenuation without internal resonance. That may be caused by the unchanged parameters in metamaterial. This law can be used to simplify the wave propagation analysis in damped nonlinear metamaterials.

Acknowledgements This work is supported by the National Natural Science Foundation of China (Nos. 12132010).

Data availability

The data that support the findings of this study are avaliable from the corresponding author [Q. Ding], upon reasonable request.

Conflict of interest

The authors declare that they have no known competing financial interests or personal relationships that could have appeared to influence the work reported in this paper.

A Comparison between the exact and the third-order approximate models

A comparison between the approximate and the exact models is here conducted to validate the accuracy of the third-order model used in this work. By utilizing the square root nonlinear force along with the dimensionless variables in Eqs. (3) and (4), the dimensionless dynamic equations of the exact model are derived as:

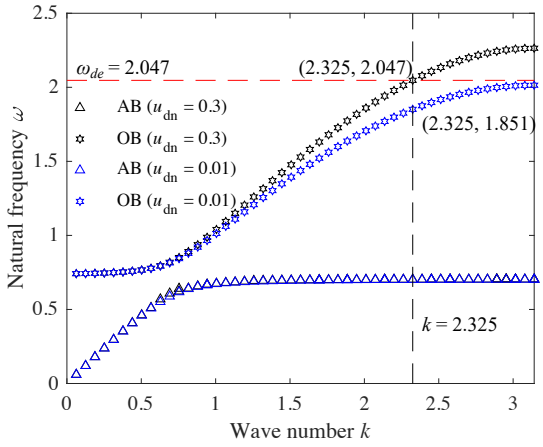

Fig. A-2 Dispersion spectrum of metamaterial with cubic nonlinear stiffness connecting lattices at $u_{dn} = 0.01$ and 0.3.

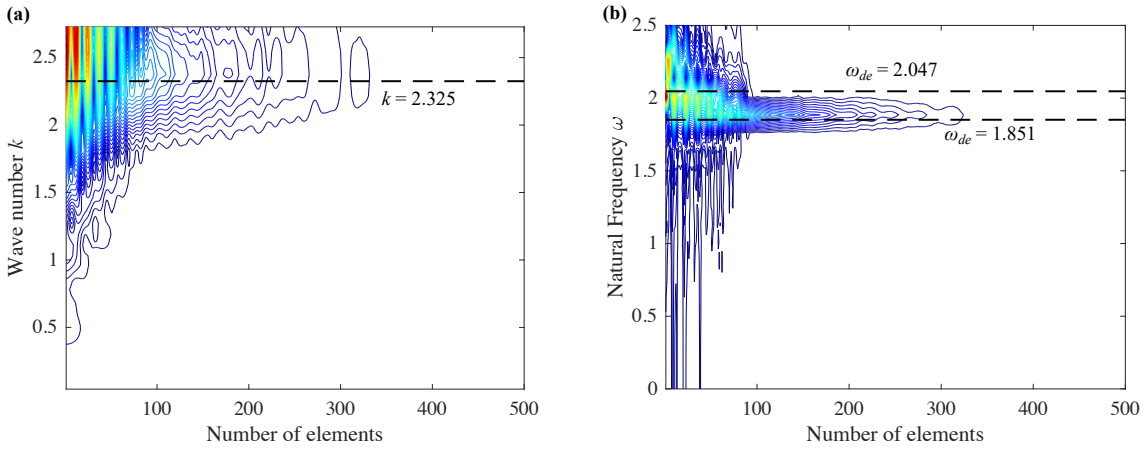

Fig. A-3 (a) Space - wavenumber and (b) space - frequency spectrum of metamaterial with cubic nonlinear stiffness connecting lattices ($A_{d0} = 0.3$, $\omega_{de} = 2.047$).

$$\begin{cases} (1+\varepsilon)\ddot{u}_{dn} + \varepsilon\ddot{v}_{dn} + 2\lambda_m\dot{u}_{dn} + 2u_{dn} - \lambda_m\left(\dot{u}_{dn-1} + \dot{u}_{dn+1}\right) - \left(u_{dn-1} + u_{dn+1}\right) = 0 \\ \varepsilon\ddot{v}_{dn} + \varepsilon\lambda_a\dot{v}_{dn} + \frac{2\varepsilon\kappa_a v_{dn}}{\sqrt{h_d^2+v_{dn}^2}}\left(\sqrt{h_d^2+v_{dn}^2} - l_d\right) = -\varepsilon\ddot{u}_{dn}, n = 1, 2, \cdots \end{cases} \tag{A-1}$$

where $\kappa_a = k_a/\varepsilon m_m\omega_m^2$, $h_d = h/x_0$, $l_d = l/x_0$. Using Eqs. (7), (A-1), and the EPMC-HBM technique, the backbone curves under five different wavenumbers $k = i\pi/5, i = 1, 2, \cdots, 5$ are represented in Fig. A-1. The results demonstrate great consistency, indicating that the third-order model can accurately predict the wave propagation characteristics. However, it is important to note that, when focusing on the high-frequency S-shaped region of S-OB, which corresponds to large displacements of the internal oscillator v_{dn}, as shown for instance in Fig. 6(d), a small difference appears between the two models, underlining the validity limit of the third-order approximation. One can note however that the frequency range in which a pronounced difference is observed, is beyond the range used in the present article, $0 < \omega < 2.5$. Therefore, it can be concluded that the third-order model sufficiently captures the essential nonlinear behaviours for all the numerical examples reported in this work.

B Variation of frequency and wavenumber during wave attenuation in nonlinear metamaterials

In Sec. 4.3, it was observed that the wavenumber of non-internally resonant waves does not change with time or wave amplitude during attenuation. This phenomenon can also be confirmed from the wave attenuation equation, see *e.g.* Eq. (22), where the wavenumber variable is completely independent and unrelated to τ and a. Although Figures 12 and 13 have preliminarily verified this phenomenon, the stable dispersion branches of the metamaterial with internal bistable oscillator are close to linear dispersion branches, and their frequencies do not significantly change with the decrease in wave amplitude. This makes the numerical examples in Sec. 4.3.2 ineffective in proving whether the above phenomenon still holds for strongly nonlinear waves that undergo significant frequency shifts. To address this issue, an additional example is provided here. The research objective is replaced with a nonlinear metamaterial in which lattices (masses set as 1) are connected by cubic nonlinear springs γ, linear springs (set as 1), and linear damping λ_m. The resonators within the lattice (mass is ε) are replaced with linear ones (stiffness and damping are $\varepsilon\kappa$ and $\varepsilon\lambda_a$) to avoid complex internal resonant responses. u_{dn} and v_{dn} represent the lattice displacement and the relative displacement of the resonator to the lattice, respectively. With these

variables, the nondimensional model of this metamaterial is the same as Eq. (7), with only the nonlinear force changed, and now reading:

$$\mathbf{F}_n = \begin{bmatrix} \gamma\left(\left(u_{dn} - u_{dn-1}\right)^3 + \left(u_{dn} - u_{dn+1}\right)^3\right) \\ 0 \end{bmatrix} \tag{A-2}$$

Assuming the parameters of the metamaterial are $\gamma = 1$, $\lambda_m = 2 \times 10^{-3}$, $\epsilon = 0.1$, $\kappa = 0.5$, $\lambda_a = 5 \times 10^{-3}$, Figure A-2 illustrates the dispersion spectrum at $u_{dn} = 0.01$ and 0.3. The results show that the optic branch experiences a hardening-type nonlinearity in the high wavenumber region. The frequency shift in this region can effectively demonstrate the variation in frequency and wavenumber during wave attenuation. Assuming an excitation frequency $\omega_{de} = 2.047$ and $A_{d0} = 0.3$, according to the dispersion spectrum, it should excite a wave with $k = 2.325$. If the wavenumber is independent of time and wave amplitude, it should remain unchanged during attenuation, with the frequency decaying to 1.851. Does the wave truly change in this manner? Figure A-3 provides the answer by the space-wavenumber spectrum and space-frequency spectrum. The results show the wavenumber does not change during attenuation, remaining at 2.325, while the frequency decreases from 2.047 to 1.851. That follows the expectation.

C The derivation of the local stability and wave attenuation equation

C.1 Local Stability

In this part, the Floquet theory is used to provide a post-processing method for determining the stability of numerical dispersion solutions from EPMC-HBM. At first, a perturbation is introduced into $\mathbf{x}_n$

$$\mathbf{x}_n = \mathbf{x}_n^0 + \Delta\mathbf{x}_n \tag{A-3}$$

where $\mathbf{x}_n^0$ is the undisturbed waveform, which can be got via the proposed algorithm, EPMC-HBM, and $\Delta\mathbf{x}_n$ represents the perturbation. By substituting Eq. (A-3) into (9) and linearizing, the following can be obtained

$$\mathbf{M}\Delta\ddot{\mathbf{x}}_n + \sum_{i=-1}^{1} \mathbf{C}_i \Delta\dot{\mathbf{x}}_{n+i} - 2\zeta\omega\mathbf{M}\Delta\dot{\mathbf{x}}_n + \sum_{i=-1}^{1} \mathbf{K}_i \Delta\mathbf{x}_{n+i} + \frac{\partial\mathbf{F}_n}{\partial\mathbf{x}_n}\left(\mathbf{x}_n^0\right)\Delta\mathbf{x}_n = \mathbf{0} \tag{A-4}$$

Eq. (A-4) is linear and can be simplified using Bloch's theorem. Assuming these perturbations meet

$$\begin{array}{l} \Delta\mathbf{x}_{n-1} = \Delta\mathbf{x}_n e^{jk}, \Delta\mathbf{x}_{n+1} = \Delta\mathbf{x}_n e^{-jk} \\ \Delta\dot{\mathbf{x}}_{n-1} = \Delta\dot{\mathbf{x}}_n e^{jk}, \Delta\dot{\mathbf{x}}_{n+1} = \Delta\dot{\mathbf{x}}_n e^{-jk} \end{array} \tag{A-5}$$

Substituting Eq. (A-5) into (A-4), the following can be derived

$$\mathbf{M}\Delta\ddot{\mathbf{x}}_n + \left(\mathbf{C}_0 - 2\zeta\omega\mathbf{M} + 2\cos k\mathbf{C}_{-1}\right)\Delta\dot{\mathbf{x}}_n + \left(\mathbf{K}_0 + 2\cos k\mathbf{K}_{-1} + \frac{\partial\mathbf{F}_n}{\partial\mathbf{x}_n}\left(\mathbf{x}_n^0\right)\right)\Delta\mathbf{x}_n = \mathbf{0} \tag{A-6}$$

Above equation can be rewritten in the state-space

$$\mathbf{y}' = \mathbf{B}\mathbf{y} \tag{A-7}$$

where

$$\mathbf{y} = \begin{bmatrix} \Delta\mathbf{x}_n \\ \Delta\dot{\mathbf{x}}_n \end{bmatrix}, \mathbf{B} = \begin{bmatrix} \mathbf{0} & \mathbf{I} \\ -\mathbf{M}^{-1}\left(\mathbf{K}_0 + 2\cos k\mathbf{K}_{-1} + \partial\mathbf{F}_n\left(\mathbf{x}_n^0\right)/\partial\mathbf{x}_n\right) & -\mathbf{M}^{-1}\left(\mathbf{C}_0 - 2\zeta\omega\mathbf{M} + 2\cos k\mathbf{C}_{-1}\right) \end{bmatrix}$$

Since $\mathbf{B}$ contains $\partial\mathbf{F}_n\left(\mathbf{x}_n^0\right)/\partial\mathbf{x}_n$ and $\mathbf{x}_n^0$ is periodic, the coefficient matrix $\mathbf{B}$ is also periodic. The stability of the dispersion solution can be determined by monodromy matrix $\mathbf{S}$ of Eq. (A-7). To derive $\mathbf{S}$, the Hsu method [68] is used here. This approach divides a period into N_t segments, fixing the periodic coefficient matrix $\mathbf{B}$ within each segment, so that the solution of Eq. (A-7) satisfies

$$\mathbf{y}_i = \exp\left(\frac{2\pi}{\omega N_t}\mathbf{B}\left(\tau_{i-1}, k\right)\right)\mathbf{y}_{i-1}, \tau_i = \frac{2\pi i}{\omega N_t} \tag{A-8}$$

And the system's monodromy matrix can be represented as

$$\begin{array}{l} \mathbf{S}(k) = \prod_{i=1}^{N_t} \mathbf{S}_i(k) \\ \mathbf{S}_i(k) = \exp\left(\frac{2\pi}{\omega N_t}\mathbf{B}\left(\tau_{i-1}, k\right)\right) \end{array} \tag{A-9}$$

It is worth noting that $\mathbf{S}$ is a periodic function of k. According to Floquet theory [29,64,68], a criterion for stability of metamaterials can be established: For $0 < k < \pi$ (considering only half of the period, as the other half is symmetrical), if the maximum absolute value of eigenvalues of $\mathbf{S}$, denoted as λ_{max}, is greater than 1, it indicates that the wave is unstable, and the larger λ_{max} implies greater instability. In addition, calculating λ_{max} is extremely time-consuming, primarily because the k corresponding to λ_{max} is unknown. To reduce the required calculating time, this work utilizes an optimization algorithm, the $fminbnd$ function in Matlab, to find out the k.

C.2 Wave Attenuation Equation

This part provides a semi-analytical wave attenuation equation using complex averaging technique. Notably, the obtained formulation only keeps accurate for non-internal resonant cases, as it is based on EPMC.

Replacing the original damping terms of Eq. (7) with artificial damping, a simplified model can be achieved

$$\mathbf{M}\ddot{\mathbf{x}}_n + 2\zeta\omega\mathbf{M}\dot{\mathbf{x}}_n + \sum_{i=1}^{1}\mathbf{K}_i\mathbf{x}_{n+i} + \mathbf{F}_n\left(\mathbf{x}_n\right) = 0 \tag{A-10}$$

According to the complex averaging technique [70], the variables $\mathbf{x}_n$ and $\dot{\mathbf{x}}_n$ are set as

$$\begin{aligned}\mathbf{x}_n &= a\frac{\mathbf{V}_n(a,\theta)+\overline{\mathbf{V}}_n(a,\theta)}{2},\\ \dot{\mathbf{x}}_n &= ja\omega\frac{\mathbf{V}_n(a,\theta)-\overline{\mathbf{V}}_n(a,\theta)}{2}\end{aligned} \tag{A-11}$$

where

$$\begin{aligned}&V_{n+i}(a,\theta) = \textstyle\sum_{m=0}^{H}\mathbf{A}_m^* e^{jm(\theta-ki)},\\ &\theta = \theta_f + \theta_s, \left(\mathbf{A}_0^* = \mathbf{A}_0/2, \mathbf{A}_m^* = \mathbf{A}_m\right)\end{aligned}$$

the $\theta_f = \omega\tau$, it denotes fast phase and θ_s represent slow phase.

Differentiating the second one in Eq. (A-11) with τ, the following can be obtained

$$\ddot{\mathbf{x}}_n = a\omega^2\frac{\mathbf{V}_n - \overline{\mathbf{V}}_n}{2} + \sum_{m=0}^{H}\mathbf{A}_m^* e^{jm\theta}a\left(j\omega\dot{a} - m\omega\left(\omega+\dot{\theta}_s\right)\right) + \sum_{m=0}^{H}j\omega\frac{\partial\mathbf{A}_m^*}{\partial a}\dot{a}ae^{jm\theta} \tag{A-12}$$

The third term in the above equation represents second-order slow variables, which are significantly smaller than the first two terms at non-bifurcation points and can therefore be neglected. By substituting the simplified Eqs. (A-12) and (A-11) into (A-10), the following can be derived:

$$a\left(\omega^2 + 2j\zeta\omega^2\right)\mathbf{M}\frac{\mathbf{V}_n - \overline{\mathbf{V}}_n}{2} + \sum_{m=0}^{H}\mathbf{M}\mathbf{A}_m^* e^{jm\theta}\left(j\omega\dot{a} - m\omega^2 a - m\omega a\dot{\theta}_s\right) + a\left(\mathbf{K}_0 + 2\cos k\mathbf{K}_{-1}\right)\frac{\mathbf{V}_n + \overline{\mathbf{V}}_n}{2} + \sum_{m=-H}^{H}\mathbf{f}_{nm}e^{jm\theta} = 0 \tag{A-13}$$

Extracting the coefficient of $e^{j\theta}$ from Eq. (A-13), then multiplying the left side by $\mathbf{A}_1^{*\mathrm{H}}$, and separating the real and imaginary parts, the following slow dynamic model can be gotten

$$\begin{cases}\dot{a} = -\zeta\omega a\\ \dot{\theta}_s = -\frac{\omega}{2} + \frac{\mathbf{A}_1^{*\mathrm{H}}\left(\mathbf{K}_0 + 2\cos k\mathbf{K}_{-1}\right)\mathbf{A}_1^*}{2\omega\mathbf{A}_1^{*\mathrm{H}}\mathbf{M}\mathbf{A}_1^*} + \frac{\mathbf{A}_1^{*\mathrm{H}}\mathbf{f}_{m1}}{\omega a\mathbf{A}_1^{*\mathrm{H}}\mathbf{M}\mathbf{A}_1}\end{cases} \tag{A-14}$$

Using the first equation in Eq. (A-14), the Eq. (A-11) can be rewritten as:

$$\mathbf{x}_{n+i} = a_0 e^{-\zeta\omega\tau}\left(\mathbf{A}_0 + \sum_{m=1}^{H}\frac{\mathbf{A}_m e^{jm(\omega\tau - ik + \theta_s)}}{2} + cc\right) \tag{A-15}$$

This equation can describe the wave attenuation process.

References

1. Y. Xiao, J. H. Wen, and X. S. Wen. Broadband locally resonant beams containing multiple periodic arrays of attached resonators. *Physics Letters A*, 376(16):1384–1390, 2012.
2. Hui Sheng, Meng-Xin He, and Qian Ding. Vibration suppression by mistuning acoustic black hole dynamic vibration absorbers. *Journal of Sound and Vibration*, 542:117370, 2023.
3. J. J. Guo, Y. Q. Li, Y. Xiao, Y. L. Fan, D. L. Yu, and J. H. Wen. Multiscale modeling and design of lattice truss core sandwich metastructures for broadband low-frequency vibration reduction. *Composite Structures*, 289, 2022.
4. D. Chronopoulos, I. Antoniadis, M. Collet, and M. Ichchou. Enhancement of wave damping within metamaterials having embedded negative stiffness inclusions. *Wave Motion*, 58:165–179, 2015.
5. I. Antoniadis, D. Chronopoulos, V. Spitas, and D. Koulocheris. Hyper-damping properties of a stiff and stable linear oscillator with a negative stiffness element. *Journal of Sound and Vibration*, 346:37–52, 2015.
6. Mauro Murer, Sawan K. Guruva, Giovanni Formica, and Walter Lacarbonara. A multi-bandgap metamaterial with multi-frequency resonators. *Journal of Composite Materials*, 57(4):783–804, 2023.
7. Z. Y. Liu, X. X. Zhang, Y. W. Mao, Y. Y. Zhu, Z. Y. Yang, C. T. Chan, and P. Sheng. Locally resonant sonic materials. *Science*, 289(5485):1734–1736, 2000.
8. H. G. Zhao, Y. Z. Liu, J. H. Wen, D. L. Yu, G. Wang, and X. S. Wen. Sound absorption of locally resonant sonic materials. *Chinese Physics Letters*, 23(8):2132–2134, 2006.
9. N. Fang, D. J. Xi, J. Y. Xu, M. Ambati, W. Srituravanich, C. Sun, and X. Zhang. Ultrasonic metamaterials with negative modulus. *Nature Materials*, 5(6):452–456, 2006.
10. J. Li and C. T. Chan. Double-negative acoustic metamaterial. *Physical Review E*, 70(5), 2004.
11. J. H. Wen, H. J. Shen, D. L. Yu, and X. S. Wen. Exploration of amphoteric and negative refraction imaging of acoustic sources via active metamaterials. *Physics Letters A*, 377(34-36):2199–2206, 2013.
12. Yang Bu, Ye Tang, and Qian Ding. Novel vibration self-suppression of periodic pipes conveying fluid based on acoustic black hole effect. *Journal of Sound and Vibration*, 567:118077, 2023.
13. Adrien Pelat, Thomas Gallot, and François Gautier. On the control of the first Bragg band gap in periodic continuously corrugated beam for flexural vibration. *Journal of Sound and Vibration*, 446:249–262, 2019.

14. Siting Hao, Hui Sheng, Xiaofei Lyu, and Qian Ding. A novel locally resonant metastructure with soft-material rings for broadband and low frequency vibration attenuation. *Engineering Structures*, 272, 2022.
15. Hui Sheng, Meng-Xin He, Jiale Zhao, Chor Ting Kam, Qian Ding, and Heow Pueh Lee. The ABH-based lattice structure for load bearing and vibration suppression. *International Journal of Mechanical Sciences*, 252:108378, 2023.
16. Yun Jing. Noise reduction using metamaterials and metasurfaces. *The Journal of the Acoustical Society of America*, 144(3):1754–1754, 2018.
17. Myung Hwan Bae and Joo Hwan Oh. Nonlinear elastic metamaterial for tunable bandgap at quasi-static frequency. *Mechanical Systems and Signal Processing*, 170, 2022.
18. Yu Xue, Jinqiang Li, Yu Wang, and Fengming Li. Tunable nonlinear band gaps in a sandwich-like meta-plate. *Nonlinear Dynamics*, 106(4):2841–2857, 2021.
19. J. R. Tempelman, A. F. Vakakis, and K. H. Matlack. Spectral energy scattering and targeted energy transfer in phononic lattices with local vibroimpact nonlinearities. *Phys Rev E*, 108(4-1):044214, 2023.
20. Gabriel Hurel, Sébastien Baguet, and Claude-Henri Lamarque. Neimark-Sacker bifurcations and non-linear energy exchange in chains of non-linear oscillators. *International Journal of Non-Linear Mechanics*, 144, 2022.
21. J. Flosi, C. H. Lamarque, and A. Ture Savadkoohi. Different dynamics of a periodic mass-in-mass nonlinear chain during a single mode excitation. *Meccanica*, 58(1):67–95, 2022.
22. Jiaxi Zhou, Lingling Dou, Kai Wang, Daolin Xu, and Huajiang Ouyang. A nonlinear resonator with inertial amplification for very low-frequency flexural wave attenuations in beams. *Nonlinear Dynamics*, 96(1):647–665, 2019.
23. Yuhao Liu, Jian Yang, Xiaosu Yi, and Dimitrios Chronopoulos. Enhanced suppression of low-frequency vibration transmission in metamaterials with linear and nonlinear inerters. *Journal of Applied Physics*, 131(10), 2022.
24. Arnaldo Casalotti, Sami El-Borgi, and Walter Lacarbonara. Metamaterial beam with embedded nonlinear vibration absorbers. *International Journal of Non-Linear Mechanics*, 98:32–42, 2018.
25. X. Fang, J. H. Wen, B. Bonello, J. F. Yin, and D. L. Yu. Ultra-low and ultra-broad-band nonlinear acoustic metamaterials. *Nature Communications*, 8, 2017.
26. X. Fang, J. H. Wen, D. L. Yu, and J. F. Yin. Bridging-coupling band gaps in nonlinear acoustic metamaterials. *Physical Review Applied*, 10(5), 2018.
27. P. Sheng, X. Fang, J. H. Wen, and D. L. Yu. Vibration properties and optimized design of a nonlinear acoustic metamaterial beam. *Journal of Sound and Vibration*, 492, 2021.
28. L. Chen, X. Liao, G. F. Xia, B. B. Sun, and Y. Zhou. Variable-potential bistable nonlinear energy sink for enhanced vibration suppression and energy harvesting. *International Journal of Mechanical Sciences*, 242, 2023.
29. H. Q. Li, A. Li, and X. R. Kong. Design criteria of bistable nonlinear energy sink in steady-state dynamics of beams and plates. *Nonlinear Dynamics*, 103(2):1475–1497, 2021.
30. D. H. Qiu, T. Li, S. Seguy, and M. Paredes. Efficient targeted energy transfer of bistable nonlinear energy sink: application to optimal design. *Nonlinear Dynamics*, 92(2):443–461, 2018.
31. T. Wang, Y. Tang, T. Z. Yang, Z. S. Ma, and Q. Ding. Bistable enhanced passive absorber based on integration of nonlinear energy sink with acoustic black hole beam. *Journal of Sound and Vibration*, 544, 2023.
32. T. Z. Wang and Q. Ding. Targeted energy transfer analysis of a nonlinear oscillator coupled with bistable nonlinear energy sink based on nonlinear normal modes. *Journal of Sound and Vibration*, 556, 2023.
33. Z. H. Wu, S. Seguy, and M. Paredes. Basic constraints for design optimization of cubic and bistable nonlinear energy sink. *Journal of Vibration and Acoustics-Transactions of the Asme*, 144(2), 2022.
34. L. I. Manevitch, G. Sigalov, F. Romeo, L. A. Bergman, and A. Vakakis. Dynamics of a linear oscillator coupled to a bistable light attachment: Analytical study. *Journal of Applied Mechanics*, 81(4), 2014.
35. Francesco Romeo, Grigori Sigalov, Lawrence A. Bergman, and Alex F. Vakakis. Dynamics of a linear oscillator coupled to a bistable light attachment: Numerical study. *Journal of Computational and Nonlinear Dynamics*, 10(1), 2015.
36. S. Benacchio, A. Malher, J. Boisson, and C. Touzé. Design of a magnetic vibration absorber with tunable stiffnesses. *Nonlinear Dynamics*, 85(2):893–911, 2016.
37. S. Lo Feudo, C. Touzé, J. Boisson, and G. Cumunel. Nonlinear magnetic vibration absorber for passive control of a multi–storey structure. *Journal of Sound and Vibration*, 438:33 – 53, 2019.
38. M. A. Al-Shudeifat and A. S. Saeed. Frequency-energy plot and targeted energy transfer analysis of coupled bistable nonlinear energy sink with linear oscillator. *Nonlinear Dynamics*, 105(4):2877–2898, 2021.
39. Y. W. Xia, M. Ruzzene, and A. Erturk. Dramatic bandwidth enhancement in nonlinear metastructures via bistable attachments. *Applied Physics Letters*, 114(9), 2019.
40. Y. W. Xia, M. Ruzzene, and A. Erturk. Bistable attachments for wideband nonlinear vibration attenuation in a metamaterial beam. *Nonlinear Dynamics*, 102(3):1285–1296, 2020.
41. C. Xu, S. Chen, C. H. Wang, Y. W. Yang, and L. Y. Zhao. Amplitude-robust metastructure with combined bistable and monostable mechanisms for simultaneously enhanced vibration suppression and energy harvesting. *Applied Physics Letters*, 122(15), 2023.
42. Han Meng, Xiuchang Huang, Yanyu Chen, Stephanos Theodossiades, and Dimitrios Chronopoulos. Structural vibration absorption in multilayered sandwich structures using negative stiffness nonlinear oscillators. *Applied Acoustics*, 182, 2021.
43. Jingyu Zhang, Jiayuan Zhang, Bohan Zhang, Yumin An, Xiao Yang, Ning Hu, Lifeng Ma, Yan Peng, and Biao Wang. Broadband multifrequency vibration attenuation of an acoustic metamaterial beam with two-degree-of-freedom nonlinear bistable absorbers. *Mechanical Systems and Signal Processing*, 212, 2024.
44. A. S. Phani, J. Woodhouse, and N. A. Fleck. Wave propagation in two-dimensional periodic lattices. *J Acoust Soc Am*, 119(4):1995–2005, 2006.
45. Yichang Shen and Walter Lacarbonara. Nonlinearity enhanced wave bandgaps in metamaterial honeycombs embedding spider web-like resonators. *Journal of Sound and Vibration*, 562, 2023.
46. Chen Gong, Xin Fang, and Li Cheng. Band degeneration and evolution in nonlinear triatomic metamaterials. *Nonlinear Dynamics*, 111(1):97–112, 2023.
47. Niels M. M. Frandsen and Jakob S. Jensen. Modal interaction and higher harmonic generation in a weakly nonlinear, periodic mass–spring chain. *Wave Motion*, 68:149–161, 2017.
48. M. D. Fronk and M. J. Leamy. Internally resonant wave energy exchange in weakly nonlinear lattices and metamaterials. *Phys Rev E*, 100(3-1):032213, 2019.
49. Smruti R. Panigrahi, Brian F. Feeny, and Alejandro R. Diaz. Wave–wave interactions in a periodic chain with quadratic nonlinearity. *Wave Motion*, 69:65–80, 2017.

50. Jianlin Yi, Zhiqiang Meng, Jianlin Chen, and Chang Qing Chen. Dispersive higher harmonic generation and enhancement in mechanical metamaterials. *International Journal of Mechanical Sciences*, 246, 2023.
51. Alessandro Fortunati, Andrea Bacigalupo, Marco Lepidi, Andrea Arena, and Walter Lacarbonara. Nonlinear wave propagation in locally dissipative metamaterials via hamiltonian perturbation approach. *Nonlinear Dynamics*, 108(2):765–787, 2022.
52. Alessandro Fortunati, Andrea Arena, Marco Lepidi, Andrea Bacigalupo, and Walter Lacarbonara. Free propagation of resonant waves in nonlinear dissipative metamaterials. *Proceedings of the Royal Society A: Mathematical, Physical and Engineering Sciences*, 480(2287), 2024.
53. Raj K. Narisetti, Massimo Ruzzene, and Michael J. Leamy. Study of wave propagation in strongly nonlinear periodic lattices using a harmonic balance approach. *Wave Motion*, 49(2):394–410, 2012.
54. M. Liu and F. Zhou. Spectro-spatial analysis of elastic wave propagation in nonlinear elastic metamaterial systems with damping. *Chaos*, 32(11):113124, 2022.
55. Soroush Sepehri, Mahmoud Mosavi Mashhadi, and Mir Masoud Seyyed Fakhrabadi. Wave propagation in fractionally damped nonlinear phononic crystals. *Nonlinear Dynamics*, 110(2):1683–1708, 2022.
56. Malte Krack. Nonlinear modal analysis of nonconservative systems: Extension of the periodic motion concept. *Computers & Structures*, 154:59–71, 2015.
57. C. Touzé and M. Amabili. Non-linear normal modes for damped geometrically non-linear systems: application to reduced-order modeling of harmonically forced structures. *Journal of Sound and Vibration*, 298(4-5):958–981, 2006.
58. C. Touzé, A. Vizzaccaro, and O. Thomas. Model order reduction methods for geometrically nonlinear structures: a review of nonlinear techniques. *Nonlinear Dynamics*, 105:1141–1190, 2021.
59. Martin Jahn, Merten Stender, Sebastian Tatzko, Norbert Hoffmann, Aurélien Grolet, and Jörg Wallaschek. The extended periodic motion concept for fast limit cycle detection of self-excited systems. *Computers & Structures*, 227, 2020.
60. Y. K. Sun, A. Vizzaccaro, J. Yuan, and L. Salles. An extended energy balance method for resonance prediction in forced response of systems with non-conservative nonlinearities using damped nonlinear normal mode. *Nonlinear Dynamics*, 103(4):3315–3333, 2021.
61. Y. K. Sun, J. Yuan, A. Vizzaccaro, and L. Salles. Comparison of different methodologies for the computation of damped nonlinear normal modes and resonance prediction of systems with non-conservative nonlinearities. *Nonlinear Dynamics*, 104(4):3077–3107, 2021.
62. Andrea Arena, Andrea Bacigalupo, and Marco Lepidi. Wave propagation in viscoelastic metamaterials via added-state formulation. *International Journal of Mechanical Sciences*, 228:107461, 2022.
63. Martin Jahn, Sebastian Tatzko, Lars Panning-von Scheidt, and Jörg Wallaschek. Comparison of different harmonic balance based methodologies for computation of nonlinear modes of non-conservative mechanical systems. *Mechanical Systems and Signal Processing*, 127:159–171, 2019.
64. T. Wang, Y. Tang, X. Y. Qian, Q. Ding, and T. Z. Yang. Enhanced nonlinear performance of nonlinear energy sink under large harmonic excitation using acoustic black hole effect. *Nonlinear Dynamics*, 111(14):12871–12898, 2023.
65. L. Meyrand, E. Sarrouy, B. Cochelin, and G. Ricciardi. Nonlinear normal mode continuation through a proper generalized decomposition approach with modal enrichment. *Journal of Sound and Vibration*, 443:444–459, 2019.
66. G.Y. Lee and Y.H. Park. A proper generalized decomposition-based harmonic balance method with arc-length continuation for nonlinear frequency response analysis. *Computers & Structures*, 275:106913, 2023.
67. Malte Krack and Johann Gross. *Harmonic Balance for Nonlinear Vibration Problems*. Springer, 2019.
68. C. Hsu. On approximating a general linear periodic system. *Journal of Mathematical Analysis and Applications*, 45(1):234–251, 1974.
69. X. Fang, J. Wen, J. Yin, D. Yu, and Y. Xiao. Broadband and tunable one-dimensional strongly nonlinear acoustic metamaterials: Theoretical study. *Phys Rev E*, 94(5-1):052206, 2016.
70. Malte Krack, Lars Panning-von Scheidt, and Jörg Wallaschek. On the computation of the slow dynamics of nonlinear modes of mechanical systems. *Mechanical Systems and Signal Processing*, 42(1-2):71–87, 2014.